International Journal of Earth Sciences (2019) 108:911–930
https://doi.org/10.1007/s00531-019-01686-x

ORIGINAL PAPER

Constraining the pressure–temperature evolution and geodynamic setting of UHT granulites and migmatitic paragneisses of the Gruf Complex, Central Alps

Jeffrey Oalmann[1,2] · Erik Duesterhoeft[3] · Andreas Möller[1] · Romain Bousquet[3]

Received: 28 August 2018 / Accepted: 31 January 2019 / Published online: 12 February 2019

Abstract
Thermodynamic modeling of compositionally mapped microdomains and whole-rock compositions is used to constrain the pressure–temperature (P–T) evolution of sapphirine granulites and migmatitic paragneisses from the Gruf Complex of the Central Alps. The P–T paths and conditions estimated from granulite microdomains and whole-rock compositions are consistent with one another, indicating that the estimates from both types of compositions are accurate. The sapphirine granulites were heated to ultra-high temperature conditions of 900–1000 °C and 7.0–9.5 kbar as they were decompressed from ca. 800 °C and 9–12 kbar, resulting in garnet breakdown. In a subsequent step, nearly isothermal decompression led to the development of cordierite-bearing coronae and symplectites. By ca. 27 Ma, the sapphirine granulites had been exhumed to the midcrustal level of the migmatitic paragneisses, which were undergoing peak metamorphism at ca. 675–750 °C and 5–7 kbar. These results are consistent with a geodynamic model that invokes heat advection to the lower crust closely following the continental-subduction (ultra-high pressure) stage of the Alpine orogeny. The most plausible geodynamic model consistent with the results of this study is breakoff of a southward subducting lithospheric slab, resulting in asthenospheric mantle flow.

Keywords UHT metamorphism · Gruf complex · Central Alps · Thermodynamic modeling · Charnockite · Sapphirine granulite

Introduction

Collisional orogens like the European Alps affect global and regional climate and host major earthquakes and magmatism. Deep geodynamic processes that occur in these settings have some control on the surface dynamics such as earthquakes. The thermal structure of orogens also regulates the volume and type of magmatism produced. Metamorphic rocks that resided in the deep crust during orogenesis and were subsequently exhumed to the surface can provide important records of the thermal and geodynamic history of the orogens in which they are found.

Ultra-high temperature (UHT) metamorphism is of particular interest in understanding the thermal evolution of orogens because of the extreme crustal conditions it requires (ca. 900–1100 °C and 7–13 kbar; Harley 1998, 2008; Brown 2007). During the Archean and Proterozoic eons, UHT metamorphism was more widespread than it has been during Phanerozoic time due to secular cooling of the Earth (Brown 2006, 2007). Therefore, attaining UHT conditions during the Phanerozoic requires geodynamic processes that result in either a high geotherm (Kelsey 2008), advection of heat from the mantle (Collins 2002; Sizova et al. 2010; Clark et al. 2011), radiogenic heating (Clark et al. 2011; Kelsey and Hand 2015), or shear heating (Kelsey 2008). Constraining the pressure–temperature–time (P–T–t) history of Phanerozoic UHT rocks can be used to elucidate the nature, timing, and intensity of these geodynamic processes.

Electronic supplementary material The online version of this article (https://doi.org/10.1007/s00531-019-01686-x) contains supplementary material, which is available to authorized users.

✉ Erik Duesterhoeft
erik.duesterhoeft@ifg.uni-kiel.de

[1] Department of Geology, The University of Kansas, 1475 Jayhawk Blvd, Lawrence, KS 66045, USA

[2] Present Address: Earth Observatory of Singapore, Nanyang Technological University, 50 Nanyang Avenue, Block N2-01B-30, Singapore 639798, Singapore

[3] Institute of Geosciences, Christian-Albrechts-Universität zu Kiel, Ludewig-Meyn-Straße 10, 24098 Kiel, Germany

However, determining the peak metamorphic conditions experienced by UHT rocks can be challenging because of retrograde elemental exchange and overprinting (e.g., Carswell and O'Brien 1993; Fitzsimons and Harley 1994; Harley 1998; Pattison et al. 2003). Therefore, techniques such as equilibrium phase diagram ("pseudosection") modeling (e.g., Pattison et al. 2003; O'Brien 2008) and accessory mineral thermometry (e.g., Watson et al. 2006; Luvizotto et al. 2009; Blackburn et al. 2012; Kooijman et al. 2012) must be employed to constrain the P–T evolution of high-grade rocks.

The Gruf Complex is enigmatic in that it hosts the only occurrence of UHT rocks in the Central Alps (Fig. 1) (Bucher-Nurminen and Droop 1983; Bousquet et al. 2012a). Therefore, understanding whether UHT metamorphism occurred during the Alpine orogeny and what processes led to it has important implications for the geodynamic history of the Central Alps. In this study, we present the results of thermodynamic modeling to constrain the P–T–t history of UHT sapphirine granulites and upper amphibolite facies migmatitic paragneisses from the Gruf Complex. The granulites are well suited for this study because they contain abundant reaction textures, which are used to constrain the P–T path. These results are used to propose a model for the geodynamic evolution of the Central Alps.

Geological setting

The European Central Alps comprise nappes that were thrust together during the Alpine orogeny (Fig. 1), which culminated in the collision of the European and Apulian plates, beginning at ca. 40 Ma (Schmid et al. 1996; Pfiffner 2016). The units that make up the Central Alps are subdivided into the Subpenninic units, which were derived from the European continental margin (Adula Nappe and Gruf Complex) and the Penninic units, which comprise the Valais (Chiavenna Ophiolite and Misox Zone) and Piemont-Liguria (Malenco unit) ocean basins and the Briançonnais (Tambo and Suretta Nappes) microcontinent (Fig. 1). Part of the Central Alps (i.e., the Southern Steep Belt; SSB in Fig. 1) has been referred to as a lithospheric mélange (Trommsdorff 1990) or tectonic accretion channel (Engi et al. 2001) in which slivers of crust (nappes) with different

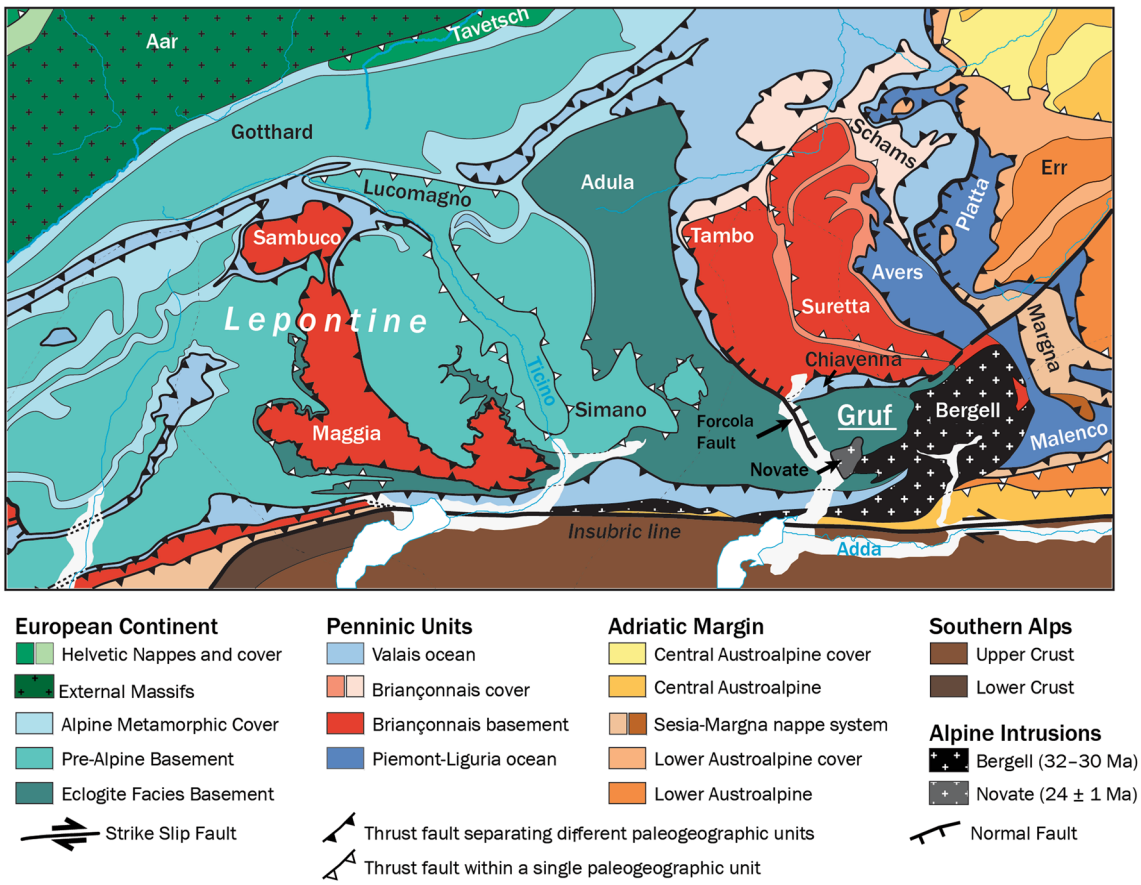

Fig. 1 Tectonic Map of the Central Alps (modified from Bousquet et al. 2012b). Ages from Bergell and Novate intrusions are from von Blanckenburg (1992) and Liati et al. (2000), respectively

paleogeographic affinities and metamorphic histories were amalgamated along shear zones during the late stages of the Alpine orogeny. Prior to the collisional event and nappe stacking, the Adula nappe and parts of the Penninic units underwent high pressure metamorphism, ranging from blueschist facies conditions in the north to ultra-high pressure (UHP) conditions in the southern Adula nappe (e.g., Gebauer 1996; Bousquet et al. 2002; Dobrzhinetskaya et al. 2002; Hermann et al. 2006; Berger and Bousquet 2008), between ca. 45 and 35 Ma (e.g., Becker 1993; Gebauer 1996; Brouwer et al. 2005; Hermann et al. 2006; Herwartz et al. 2008; Sandmann et al. 2014 and see; Berger and Bousquet 2008 for a review). This was a result of subduction of the ocean basins, Briançonnais microcontinent, and edge of the European continental margin (e.g., Stampfli et al. 1998; Berger and Bousquet 2008). After exhumation of the (U)HP units, a large part of the Central Alps (the Lepontine Dome) experienced Barrovian metamorphism between 32 and 22 Ma (Rubatto et al. 2009; Berger et al. 2011), ranging from greenschist facies in the north to sillimanite-zone migmatization in the south (Todd and Engi 1997; Frey and Ferreiro Mählmann 1999; Burri et al. 2005). In the southeastern Central Alps, the granodiorite to tonalite Bergell Intrusion was emplaced along the Insubric line, which is part of the Periadriatic fault system, between 32 and 30 Ma (von Blanckenburg 1992; Samperton et al. 2015) (Fig. 1). Magmatism in the Central Alps waned after the intrusion of the Novate leucogranite at 24 ± 1.2 Ma (Liati et al. 2000).

The Gruf Complex occurs at the eastern extent of the Central Alps (Fig. 1) where it is bordered to the north by the Chiavenna ophiolite (Valais) and Tambo nappes (Briançonnais). In the south and east, it is structurally overlain by the Bergell Intrusion (Berger et al. 1996; Davidson et al. 1996). The normal-sense Forcola fault (Ciancaleoni and Marquer 2006) separates the Gruf Complex from the Adula nappe, which experienced UHP metamorphism (Heinrich 1986; Gebauer 1996; Dobrzhinetskaya et al. 2002; Krogh Ravna and Terry 2004). The Novate leucogranite intruded the southwestern part of the Gruf Complex along the Forcola fault at 24 ± 1.2 Ma (Liati et al. 2000).

The Gruf Complex comprises mostly migmatitic biotite orthogneisses with more scarce garnet + sillimanite + biotite ± muscovite migmatitic paragneisses and biotite–poor leuco-orthogneisses (detailed mapping by Galli et al. 2013; Fig. 2). The contact of leuco-orthogneiss to migmatitic biotite orthogneiss is diffuse, whereas the contact to migmatitic paragneiss is either intrusive, sharp or irregular. Boudinaged charnockitic sheets are separated from the biotite orthogneiss by local, up to 50 cm-wide, competence-driven mylonitic shear zones with

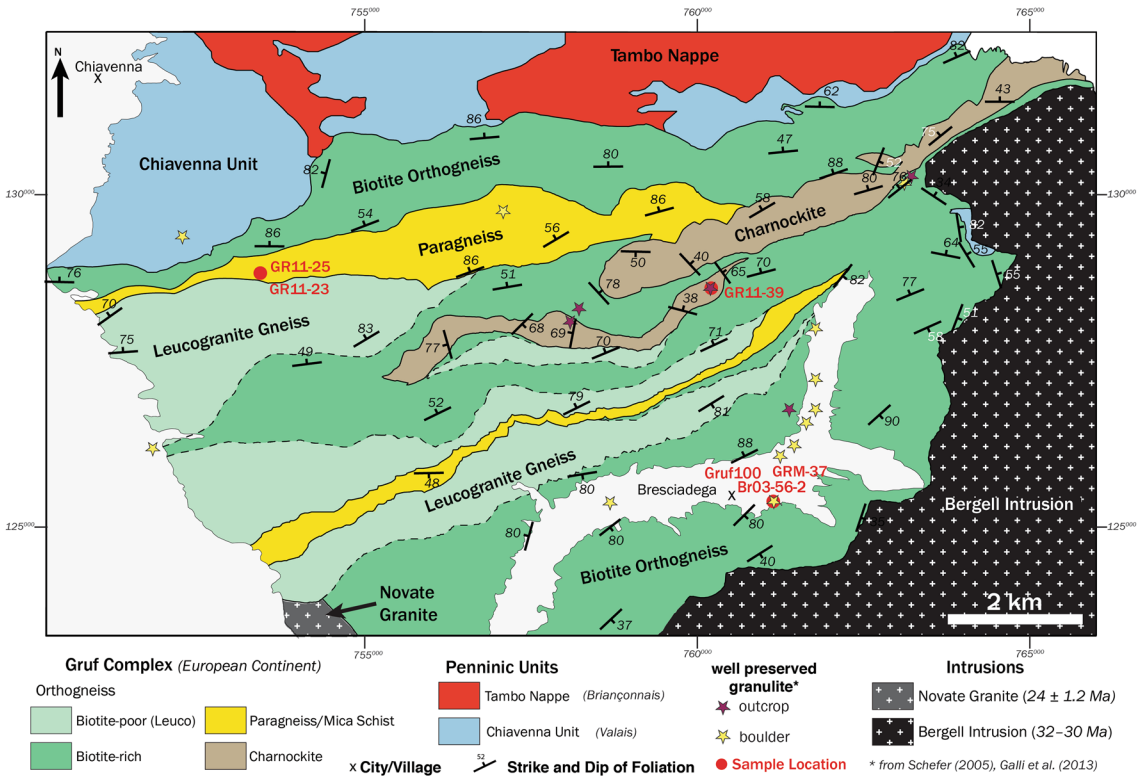

Fig. 2 Geologic map of the Gruf Complex showing locations of samples used in this study (modified from Galli 2010). Dashed lines show diffuse contacts

reverse-sinistral shear sense (Galli et al. 2013). The two largest of these charnockite bodies crop out along a high ridge at the center of the Gruf Complex (Fig. 2). Schmid et al. (1996) interpret the structures of the Gruf complex as two antiforms (where the two paragneiss-bodies define the NE-plunging fold axes of the antiforms; see also Galli et al. 2013). Scarce Mg- and Al-rich, sapphirine-bearing granulites occur as pods, rafts, and schlieren within the charnockites. Variably deformed felsic dikes, ranging from biotite-granite to beryl + garnet + biotite + muscovite pegmatite, occur throughout the Gruf Complex. The older, muscovite-free and muscovite-poor dikes are deformed whereas the younger, muscovite-rich dikes are undeformed.

Nicollet et al. (2018) used texturally controlled U-Pb monazite and zircon dating to conclude that UHT metamorphism of the granulites occurred during Alpine orogenesis, with monazite dates constraining the timing of peak to post-peak metamorphism between 34 and 30 Ma. Oalmann (2017) used texturally controlled zircon petrochronology to conclude that there was minor zircon growth in equilibrium with garnet at 34.8 ± 1.1 Ma; zircon was partly resorbed during UHT metamorphism, and zircon rims crystallized during early retrograde metamorphism and melt crystallization (ca. 700–800 °C) at 32.7 ± 0.5 Ma (Liati and Gebauer 2003). He used the U-Pb zircon ages of variably deformed felsic dikes to conclude that the UHT granulite/charnockite units were juxtaposed against the migmatitic ortho- and paragneisses along mylonitic shear zones between 30 and 27 Ma, that contractional deformation ended by 25.6 ± 0.3 Ma, and that decompression led to crustal melting between 26 and 24 Ma (see also Liati et al. 2000). Oalmann (2017) also determined that the granulites and charnockites cooled from 700 to 420 °C between ca. 30 and 19 Ma using U-Pb rutile thermochronology.

Sample descriptions

Leucogranulite (GR11–39)

Sample GR11–39 is a felsic granulite enclave within charnockite characterized by alternating light and dark bands, which define a gneissosity (Figs. 3a, 4a). Quartz within the leucosomes (light bands) is characterized by a bimodal grain size distribution. Large quartz ribbons (up to 1 cm long) exhibit undulose extinction and are elongate subparallel to the gneissosity. Smaller quartz grains are equant and have lobate grain boundaries. Blocky plagioclase grains are elongate subparallel to the gneissosity and lineation defined by the large quartz porphyroclasts. Lens-like K-feldspar porphyroclasts are also elongate subparallel to the gneissosity. Garnet and biotite occur scarcely within the leucosomes.

The melanosomes consist of biotite, garnet, orthopyroxene, sapphirine, and minor spinel and rutile. Biotite occurs as elongate blades that are oriented subparallel to the gneissosity. Anhedral to subhedral garnet porphyroblasts (up to 1 mm in diameter) commonly have embayments filled with individual grains or symplectites of plagioclase ± orthopyroxene ± biotite ± sapphirine ± spinel (Fig. 5a). Outside of the garnet embayments, blocky orthopyroxene occurs as isolated porphyroblasts. Up to 3 mm-long aggregates of sapphirine (± spinel) are aligned subparallel to the gneissosity and are typically isolated from the other mafic minerals except for biotite (Fig. 4a). The relative proportion of the phases varies from layer to layer. Some melanosome layers consist mainly

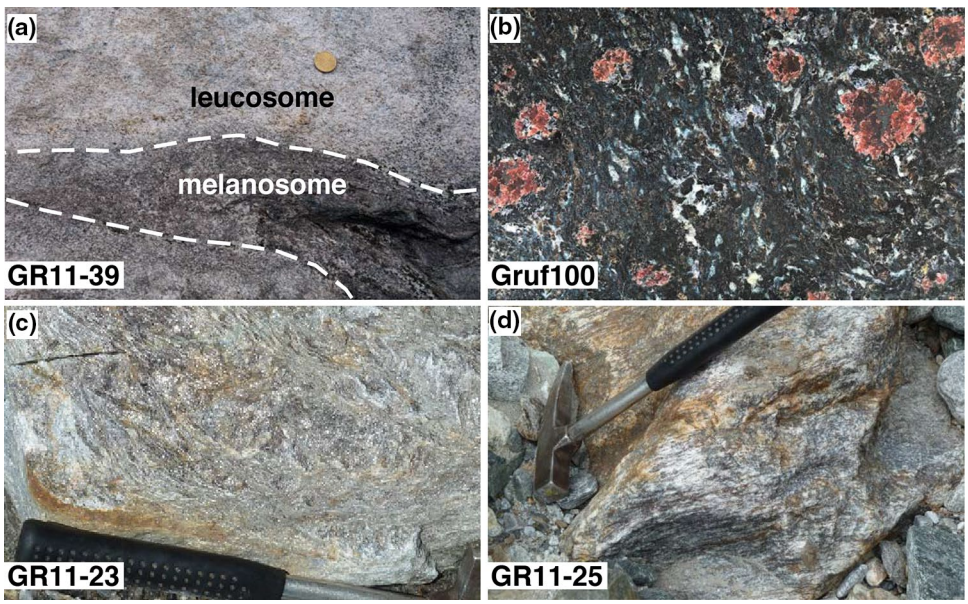

Fig. 3 Sample photos: **a** Leucogranulite sample GR11–39. **b** Resdiual granulite sample Gruf100. White patches are crystallized partial melt, comprising quartz + K-feldspar + plagioclase. **c** Muscovite-bearing migmatitic paragneiss sample GR11–23. **d** Muscovite-free migmatitic paragneiss sample GR11–25

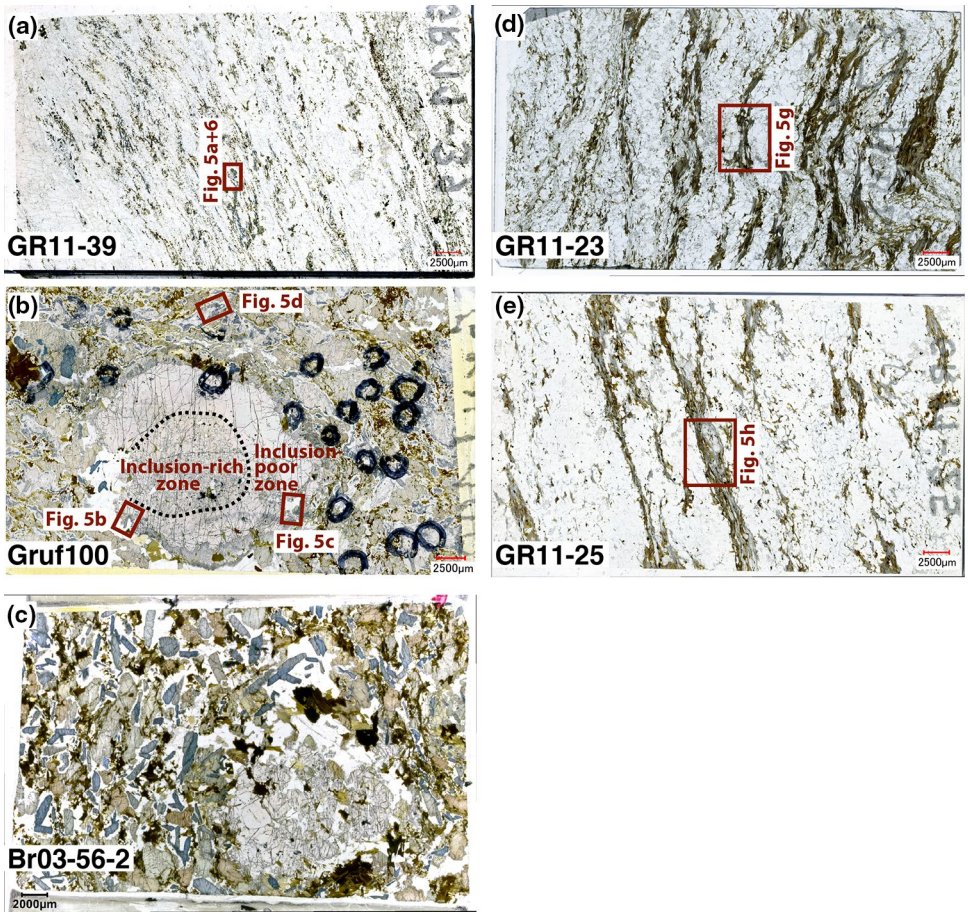

Fig. 4 Scans of thin sections that were used in this study: **a** Leucogranulite sample GR11–39. **b** Resdiual granulite sample Gruf100. **c** Residual granulite sample Br03-56-2. **d** Muscovite-bearing migmatitic paragneiss sample GR11–23. **e** Muscovite-free migmatitic paragneiss sample GR11–25

of elongate biotite with or without sapphirine ± spinel aggregates, whereas other layers are dominated by blocky orthopyroxene. Garnet occurs as isolated porphyroblasts within the melanosomes.

In this study, a garnet embayment filled with symplectites of orthopyroxene, plagioclase, sapphirine, and spinel (Fig. 5a) is investigated. This garnet-breakdown texture is surrounded by quartz + K-feldspar, which is interpreted to be crystallized melt. This type of texture is common in the leucogranulite samples and, to a lesser extent, in the charnockites.

Residual granulite (Gruf100)

Residual granulite sample Gruf100 is a garnet-rich orthopyroxene + sapphirine + biotite + sillimanite + cordierite granulite boulder, found in the outcrop area of the orthogneisses, that lacks a definite fabric (Figs. 3b, 4b). The distribution of the constituent minerals in the hand sample scale is homogeneous (Fig. 3b).

Garnet porphyroblasts are subhedral and range from 3 mm to 2 cm in diameter (Fig. 3b). The largest of these porphyroblasts are characterized by inclusion-rich cores and inclusion-poor rims (Fig. 3b). Embayments in garnet are filled with crystallized leucosome (quartz + feldspar), blocky orthopyroxene porphyroblasts, bladed sapphirine, biotite, cordierite, and/or symplectites consisting of orthopyroxene ± sapphirine ± cordierite (Fig. 5b, c).

Subhedral orthopyroxene porphyroblasts range from 1 to 8 mm. In many cases, orthopyroxene and bladed sapphirine are intergrown (Fig. 5c). In the more biotite-rich parts of the sample, biotite occurs along the edge and within cracks of orthopyroxene (Fig. 5d).

Bladed sapphirine porphyroblasts range from < 1 mm to 5 mm in length. These porphyroblasts are most common near garnet and orthopyroxene (Fig. 5b, c), but also occur within leucosomes. There are no inclusions of sapphirine within the garnet.

Prismatic sillimanite porphyroblasts reach ca. 3 mm in length and are invariably (at least partly) surrounded by sapphirine + cordierite + minor spinel symplectites, which are separated from orthopyroxene by cordierite coronae (Fig. 5d). These textures likely formed from a reaction such as sillimanite + orthopyroxene = sapphirine + cordierite + spinel. In some cases, sillimanite occurs as aggregates made up of numerous small prisms that together form a blade-like shape (Fig. 5d). This may be the result of sillimanite pseudomorphing kyanite.

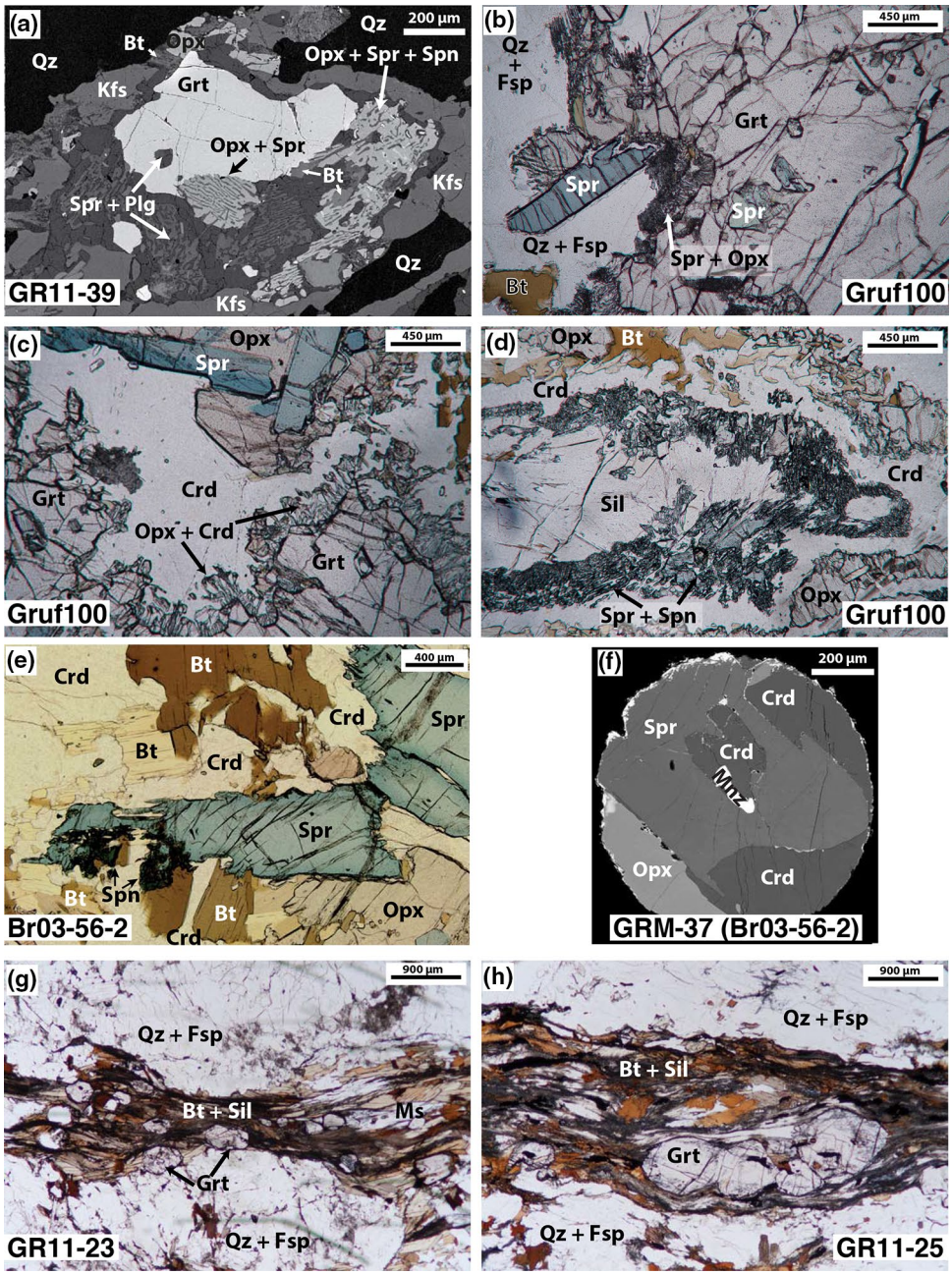

Fig. 5 Photomicrographs (colored) and backscattered electron (BSE) (black and white) images of textures in the granulites and paragneisses: **a** BSE image of garnet breakdown texture from leucogranulite sample GR11–39. **b** Photomicrograph from residual granulite sample Gruf100 showing embayment in garnet filled with prismatic sapphirine, sapphirine + orthopyroxene symplectites and quartz + feldspar, which represents crystallized melt. **c** Photomicrograph from residual granulite sample Gruf100 showing intergrown sapphirine and orthopyroxene porphyroblast separated from garnet by cordierite moat. Garnet is also fringed with orthopyroxene + cordierite symplectites. **d** Photomicrograph from residual granulite sample Gruf100 showing large sillimanite porphyroblast rimmed by sapphirine + spinel + cordierite symplectite, which is separated from orthopyroxene and biotite by a cordierite corona. **e** Photomicrograph from residual granulite sample Br03-56-2 showing a large sapphirine porphyroblast fringed by fine-grained spinel aggregates surrounded by cordierite, biotite, and orthopyroxene. **f** BSE image of texture GRM-37 from residual granulite sample showing orthopyroxene, sapphirine, cordierite, and monazite. **g** Photomicrograph from muscovite-bearing migmatitic paragneiss sample GR11–23 showing typical leucosomes and melanosome, consisting of biotite, muscovite, sillimanite, and garnet. **h** Photomicrograph from muscovite-free migmatitic paragneiss sample GR11–25 showing typical leucosomes and melanosome, consisting of biotite, sillimanite, and aggregate of garnet porphyroblasts that are aligned subparallel to the foliation/gneissosity

Cordierite occurs in orthopyroxene-bearing symplectites or as coronae around and between garnet, orthopyroxene, sapphirine (Fig. 5b, c) and sillimanite porphyroblasts (Fig. 5d). In some areas of the thin section, cordierite is so abundant that the other mafic and aluminosilicate phases (garnet, orthopyroxene, sapphirine, and sillimanite) do not touch one another. We interpret these relationships to indicate that cordierite formed shortly after orthopyroxene and sapphirine. Biotite mostly consists of small masses that surround orthopyroxene and garnet (Fig. 5d). However, large aggregates of biotite are also present. Based on the relationship of biotite to the other phases, we interpret biotite to be a retrograde phase. Leucosomes occur as discrete, ≤ 2 cm, white to gray pods comprising quartz + K-feldspar + plagioclase (Figs. 3b, 4b). The feldspars in these leucosomes lack perthitic texture, and plagioclase and K-feldspar occur in roughly equal proportions. Minor blocky plagioclase also occurs outside of the leucosomes in garnet embayments.

Residual granulite (Br03-56-2)

Another residual granulite boulder sample found in the outcrop area of the orthogneisses was also modeled. The whole rock composition that was used for the input of this sample was taken from the Diploma Thesis of Schefer (2005). This residual granulite has a very similar appearance to the other residual granulite sample (Gruf100) in terms of its constituent minerals and their grain sizes, habits, and relationships to one another (Fig. 4c). The main petrographic differences are that this sample lacks sillimanite (except for sillimanite exsolution lamellae in orthopyroxene) and contains a higher proportion of spinel and biotite than sample Gruf100. Spinel occurs either as inclusions in or at the fringes of garnet or as fine-grained aggregates that fringe sapphirine (Fig. 5e).

Residual granulite (GRM-37)

A monazite-bearing domain, which was extracted from a thin section of residual granulite sample Br03-56-2, contains orthopyroxene, sapphirine, and cordierite (Fig. 5f). The monazite grain occurs with cordierite as part of a two-phase inclusion in sapphirine (Fig. 5f). This monazite grain was dated by Oalmann (2017) using Laser Ablation Inductively Coupled Plasma Mass Spectrometry (LA-ICP-MS) and yields a weighted mean $^{206}Pb/^{238}U$ age of 32.5 ± 0.5 Ma based on three analyses.

Migmatitic paragneiss (GR11–23)

Sample GR11-23 is a garnet + sillimanite + biotite + muscovite paragneiss that has well-developed gneissic banding defined by segregations of quartzofeldspathic and garnet–sillimanite–biotite–muscovite-rich layers (Figs. 3c, 4d). This sample exhibits a well-developed crenulation cleavage defined by folding of the gneissic banding and folds within the mica-rich layers (Figs. 3c, 4d). Muscovite, biotite, and fibrolitic sillimanite are the most abundant minerals in the dark layers, whereas garnet is scarcer (Fig. 5g). Euhedral garnet porphyroblasts are elongate subparallel to the gneissosity in some cases, but in most cases garnet is equant (Fig. 5g). Quartz has a bimodal size distribution in which the largest grains have chessboard-type undulose extinction and are elongate subparallel to the gneissosity. Smaller quartz grains have lobate grain boundaries and typically have similar extinction angles. K-feldspar occurs as augen within the leucosome, and plagioclase typically has a blocky habit.

Migmatitic paragneiss (GR11–25)

Sample GR11–25 is a migmatitic garnet + sillimanite + biotite paragneiss that has well-developed gneissosity, which is defined by segregation of quartzofeldspathic and garnet-, sillimanite-, and biotite-rich layers (Figs. 3d, 4e). This sample consists of a higher proportion of leucosome than sample GR11-23 (Fig. 4d, e). Aggregates of biotite and sillimanite are elongate subparallel to the gneissosity (Fig. 5h). Euhedral garnet porphyroblasts are mainly restricted to the melanosome layers and are elongate subparallel to the gneissosity in some cases (Fig. 5h). Quartz has a similar bimodal size distribution and microstructural attributes as the quartz in the other paragneiss sample. The leucosomes of this sample comprise a higher proportion of plagioclase and a lower proportion of K-feldspar than the leucosomes in sample GR11-23.

Methods

Electron probe microanalysis (EPMA)

Quantitative major element compositions were collected with a JEOL Superprobe JXA-8900R electron microprobe at Christian Albrechts Universität zu Kiel (Online Resource Table S1). An accelerating voltage of 15–20 kV and a beam current of 20 nA were used for the analyses, and the CITZAF method of Armstrong (1995) was used to correct the data. X-ray compositional maps were obtained using a 15 kV accelerating voltage, 10–40 nA beam current, and 80–200 ms dwell time. Backscattered electron (BSE) images were used with the JEOL Image-Archive software to determine the area percent of the phases comprised in the chemical microdomains. The bulk compositions of these microdomains were then calculated by comparing the intensity (counts) of X-ray compositional maps with the quantitative EPMA spot analyses (weight percent) (Online Resource Table S2).

X-ray fluorescence (XRF)

Between 5 and 10 kg of sample (excluding weathered exteriors) was crushed and powdered using a steel plated jaw crusher and ball mill at the University of Kansas, Department of Geology. Splits of the powder were sent to the GeoAnalytical Lab at Washington State University for major and trace element analyses (Online Resource Table S2). Further powdering of the samples, fusing into glass beads, and analysis by XRF were carried out following the methods of Johnson et al. (1999).

LA-ICP-MS

Garnet trace element compositions were measured using laser ablation inductively coupled mass spectrometry (LA-ICP-MS) at the University of Kansas, Department of Geology's Isotope Geochemistry Lab. The analytical protocols that were used for the measurements are shown in Online Resource Table S3.

Pressure–temperature modeling

Equilibrium phase diagrams (commonly referred to as "pseudosections") were calculated for whole-rock samples (residual granulites and migmatitic paragneisses; Online Resource Table S2) and microtextural domains (Online Resource Table S2) of the granulites using Theriak-Domino version 04.02.2017 (De Capitani 1994; De Capitani and Petrakakis 2010). The whole-rock compositions of the residual granulite samples (Gruf-100 and Br03-56-2) were used as the input for the phase diagram calculations because of the homogeneous distribution of phases in these samples.

In the leucogranulite sample (GR11–39), the effective compositions of symplectite reaction textures are not represented by the whole-rock composition because the subsolidus reactions are separated from one another by melt. Therefore, the input compositions for these symplectite reaction textures were calculated by combining the BSE image, X-ray composition maps, and EPMA spot analyses of the area comprising the reaction texture as described above. This method was also used to calculate the composition of a monazite-bearing domain (GRM-37), which was drilled for monazite dating from a thin section of residual granulite sample Br03-56-2. The area shown in Fig. 5f comprising Opx, Crd and Spr is the domain that was used as input composition. Consequently, pressure–temperature conditions estimated by microdomain modeling give information on symplectite formation.

The Theriak-Domino database tcds55_p07 (downloaded from dtinkham.net/peq.html), which consists of thermodynamic data from Holland and Powell (1998), was used for all calculations. The following mineral solution models were used: talc, epidote, staurolite, chlorite, chloritoid, and cordierite (Holland and Powell 1998); white mica (Coggon and Holland 2002); orthopyroxene and spinel (White et al. 2002); feldspar (Holland and Powell 2003); sapphirine and osumilite (Kelsey et al. 2004); biotite, garnet, and ilmenite (White et al. 2005); melt for metapelitic compositions (White et al. 2007); amphibole and clinopyroxene (Diener and Powell 2012). The H_2O content of all compositions was estimated using temperature versus mole fraction hydrogen M_H ($=0.5\times M_{H2O}$) binary phase diagrams (Fig. A1 in Online Resource S4). See Online Resource S4 for details.

Garnet compositional zoning

The major element zoning patterns of the garnet from the modeled reaction texture in the leucogranulite sample *GR11–39* are shown in the X-ray compositional maps in Fig. 6 (quantitative data in Online Resource Table S1). Figure 7 shows profiles of compositional zoning in the garnet porphyroblast from the reaction texture in the leucogranulite sample *GR11–39*. The grossular component of this garnet is strongly zoned (Fig. 6a). Mole fraction grossular ($X_{grossular}$) decreases from 0.1 in the core to 0.03 in the rim (Fig. 7). There is no strong zoning with respect to the other major cations (Mg, Fe, and Mn; Fig. 6b, c, d) except for a minor rimward decrease in Mg (rim $X_{pyrope}=0.36$, whereas core $X_{pyrope}=0.40$) and a minor rimward increase in Fe (rim $X_{almandine}=0.62$, whereas core $X_{almandine}=0.49$) along one edge, which is in contact with biotite (Fig. 7). Along all other edges of the garnet, X_{pyrope} (0.44) and $X_{almandine}$ (0.53) increase slightly (Figs. 6, 7). The spessartine component is invariable throughout ($X_{spessartine}=0.01$).

Pressure–temperature estimates

Leucogranulite (GR11–39)

A garnet-breakdown domain (Fig. 5a), which is representative of garnet textures in the leucogranulite samples, was targeted in sample GR11–39. The observed assemblage of garnet + orthopyroxene + plagioclase + sapphirine + spinel + melt (represented by quartz + K-feldspar) is stable at ca. 900–1050 °C and 6–9 kbar on the calculated phase diagram (Fig. 8a). The garnet compositional isopleths that correspond to the measured composition of the garnet core ($X_{grossular}=0.06$–0.11 and $X_{pyrope}=0.4$) intersect at ca. 800 °C and 9–12 kbar, which is well outside the stability field of the observed assemblage (Fig. 8e). The calculated isopleths of garnet volume decrease (from 25–20 to 15 vol%) between the intersection of the garnet compositional isopleths and the stability field of the observed assemblage

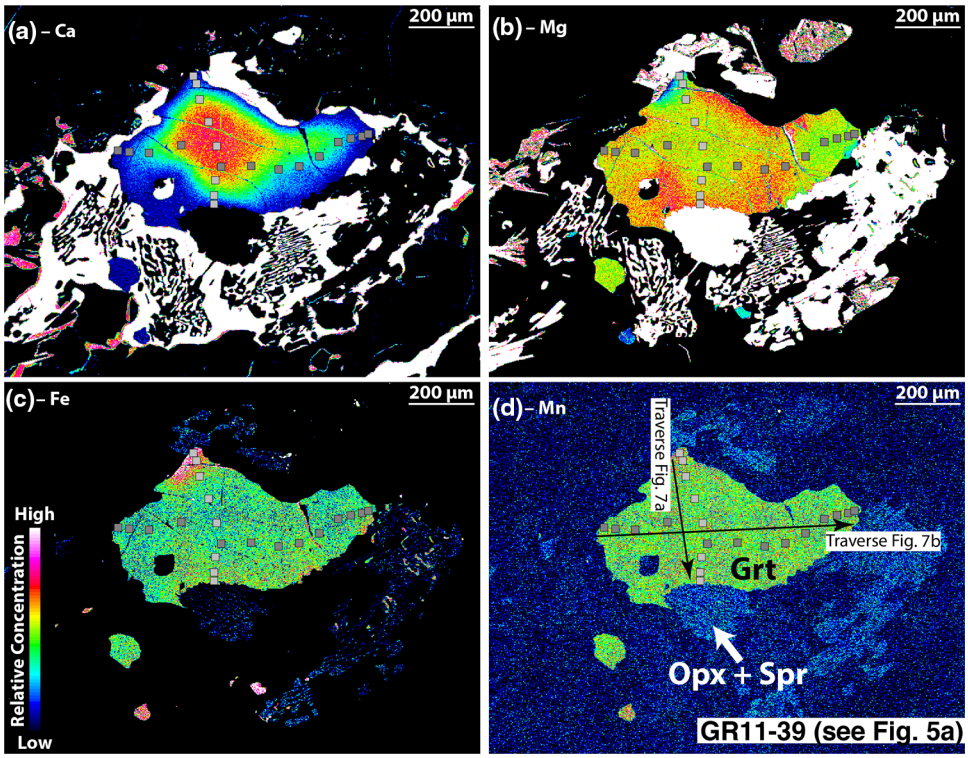

Fig. 6 X-ray composition maps of the modeled reaction texture in the leucogranulite sample GR11–39: **a** Relative Ca concentration. **b** Relative Mg concentration. **c** Relative Fe concentration. **d** Relative Mn concentration. Grey squares show the location of the quantitative EPMA spot analyses (Online Resource Table S1). Light grey squares are part of the vertical traverse. Dark grey squares are part of the horizontal traverse (see Fig. 7)

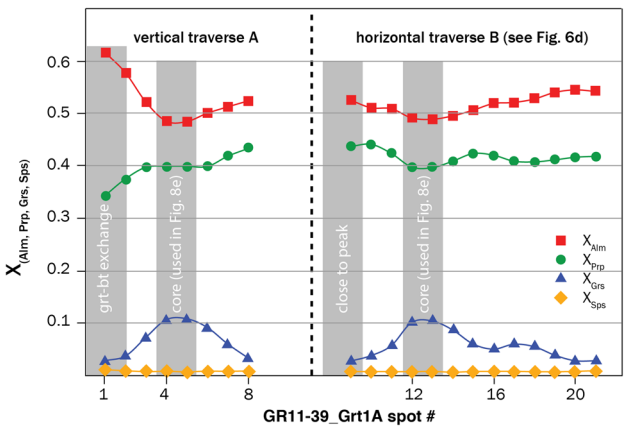

Fig. 7 Chemical zoning profile of a garnet porphyroblast from leucogranulite sample GR11–39. The traverse locations are shown in Fig. 6d. Quantitative EPMA spot analyses of grain GR11-39_Grt1A are listed in Online Resource Table S1

(Fig. 8f), indicating that orthopyroxene, plagioclase, sapphirine, and spinel formed at the expense of garnet. The relative positions of the stability fields of sapphirine and orthopyroxene indicate that sapphirine grew earlier than orthopyroxene (see also Fig. 11a). This is consistent with the textural relationships between the phases and the anhedral shape of the garnet. Therefore, we interpret that the rock underwent heating to UHT conditions during decompression from near-eclogite facies conditions along the P–T path shown in Fig. 8f.

Residual granulites (Gruf100 + Br03-56-2)

The peak assemblage of residual granulite sample Gruf100 is interpreted to be K-feldspar + garnet + orthopyroxene + sapphirine + sillimanite + rutile + melt. This assemblage is stable at 925–975 °C and 8.25–10.25 kbar on the calculated phase diagram (Fig. 8b). The presence of sapphirine + orthopyroxene symplectites and cordierite coronae around garnet (Fig. 5b–d) suggests that garnet was breaking down at peak conditions. Cordierite was stable at lower pressure than the interpreted peak assemblage (Fig. 8b), suggesting that moats of cordierite around garnet, orthopyroxene, sapphirine, and sillimanite formed during continued decompression. Sapphirine + cordierite symplectites around sillimanite porphyroblasts also suggest decompression to less than ca. 8.5 kbar (the edge of the sillimanite stability field) occurred prior to significant cooling (Fig. 8b, g). The biotite-out reaction occurs very close to the stability field of the peak assemblage. Therefore, it is likely that some of the biotite did not react out completely at peak conditions and resumed growth shortly after cooling commenced. Garnet volume-percent isopleths (Fig. 8g) indicate that garnet volume was highest at higher pressures and lower temperatures than the stability field of the peak assemblage, indicating that peak

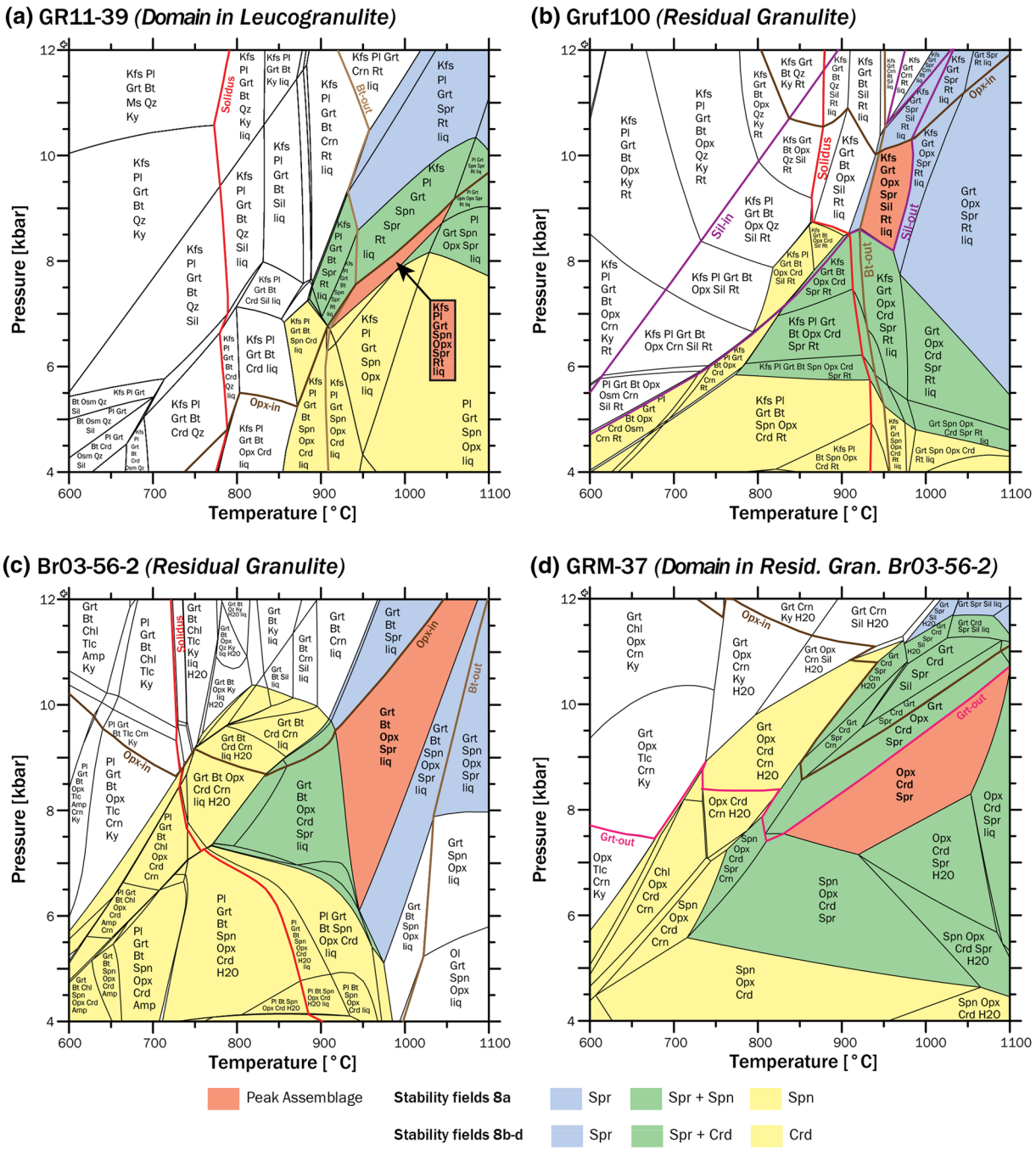

Fig. 8 **a–d** Equilibrium phase diagrams calculated for granulite samples and reaction textures. **e** P–T diagram showing peak field and garnet compositional isopleths (X_{pyrope} and $X_{grossular}$) calculated for the garnet breakdown texture in leucogranulite sample GR11–39. The red bar represents the range of measured compositions in the garnet. **f** P–T diagram with peak field and garnet volume percent isopleths for the garnet breakdown texture in leucogranulite sample GR11–39. The P–T path is drawn from the garnet compositional range from **e** to the peak field, indicating a decrease of garnet volume during decompression and heating. **g** P–T diagram with peak field and garnet volume percent isopleths for the residual granulite sample Gruf100. The starting point of the P–T path coincides with the maximum pressure starting point in **f**, and the path is drawn to indicate a decrease in garnet volume during decompression and heating and continued nearly isothermal decompression through the stability field of the peak assemblage into the cordierite stability field. **h** P–T diagram with peak field and garnet volume percent isopleths for the residual granulite sample Br03-56-2. The P–T paths are drawn to indicate a decrease in garnet volume during decompression and heating to peak conditions. The starting point coincides with the maximum pressure starting point in **f**. The P–T path also considers the growth of spinel after sapphirine and crosses into the cordierite stability field (**c**). Note that the stability of osumilite (**a, b**) at medium temperature (600–700 °C) is due to the low amount of water in the calculation (not representing the retrograde state) and may be an artifact

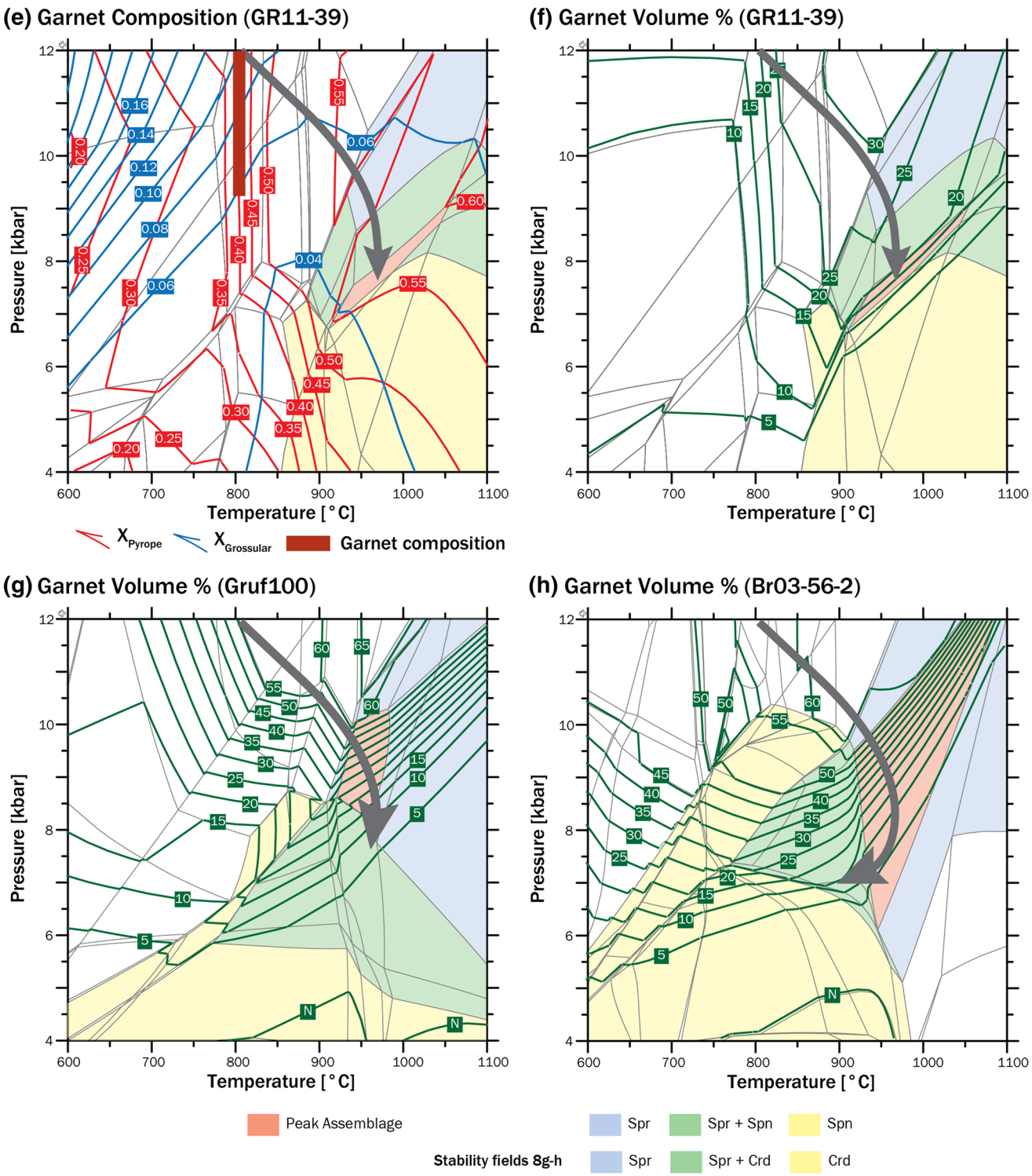

Fig. 8 (continued)

conditions were reached during decompression. Garnet-breakdown during retrograde cooling does not seem plausible because such a path would follow the garnet volume-percent isopleths (Fig. 8g). Based on these observations, we interpret that this sample followed the P–T path shown in Fig. 8g in which garnet-breakdown and heating to UHT conditions occurred during decompression, and nearly isothermal decompression continued to < 8.5 kbar.

The interpreted peak assemblage of residual granulite sample Br03-56-2 (garnet + othropyroxene + biotite + sapphirine + spinel + melt) is stable over a large area (925–1075 °C and 6 to > 11 kbar) of the P–T phase diagram (Fig. 8c). This sample also shows textural evidence for garnet breaking down to form orthopyroxene, sapphirine, and cordierite (Fig. 4c) similar to that in residual granulite sample Gruf100, and garnet volume-percent isopleths (Fig. 8h) also indicate a higher garnet volume percent at higher pressure and lower temperature than the stability field of the peak assemblage. The beginning of the P–T path shown in Fig. 8h represents a combination of the P–T paths determined for the leucogranulite garnet-breakdown texture (Fig. 8f) and other residual granulite sample (Fig. 8g). However, in contrast to sample Gruf100, the cordierite moats in sample Br03-56-2 probably formed in response to cooling rather than decompression according to the phase diagram (Fig. 8c), indicating that the slope of the P–T path became shallower (i.e., cooling became more dominant than decompression) at ca. 7 kbar.

Based on the straight grain boundaries between phases and intergrown nature of sapphirine and cordierite (Fig. 5f), we interpret the phase relationships within microdomain GRM-37 to represent equilibrium. The observed assemblage of orthopyroxene + sapphirine + cordierite was stable at 850–1100 °C and 7.25–10.5 kbar (Fig. 8d). The P–T estimates from the whole rock composition of residual granulite sample Br03-56-2 and the microdomain composition of texture GRM-37, which was drilled from sample Br03-56-2, overlap considerably (Fig. 8c, d).

Migmatitic paragneisses (GR11-23 + GR11-25)

The calculated phase diagram for the garnet + sillimanite + biotite + muscovite paragneiss (sample GR11–23) indicates that the observed peak assemblage (plagioclase + garnet + biotite + muscovite + quartz + sillimanite + ilmenite + melt) was stable at ca. 650–750 °C and 4.0–7.5 kbar (Fig. 9a). Sample GR11-25 is mineralogically and texturally similar to sample GR11-23, but it lacks muscovite and has a higher proportion of leucosome. However, the stability field of the observed peak assemblage (675–750 °C and 5–7 kbar) overlaps considerably with that of the muscovite-bearing sample (Fig. 9a, b). We interpret this to indicate that the difference in mineralogy reflects the slight difference in the bulk rock composition of these samples and not differences in peak P–T conditions.

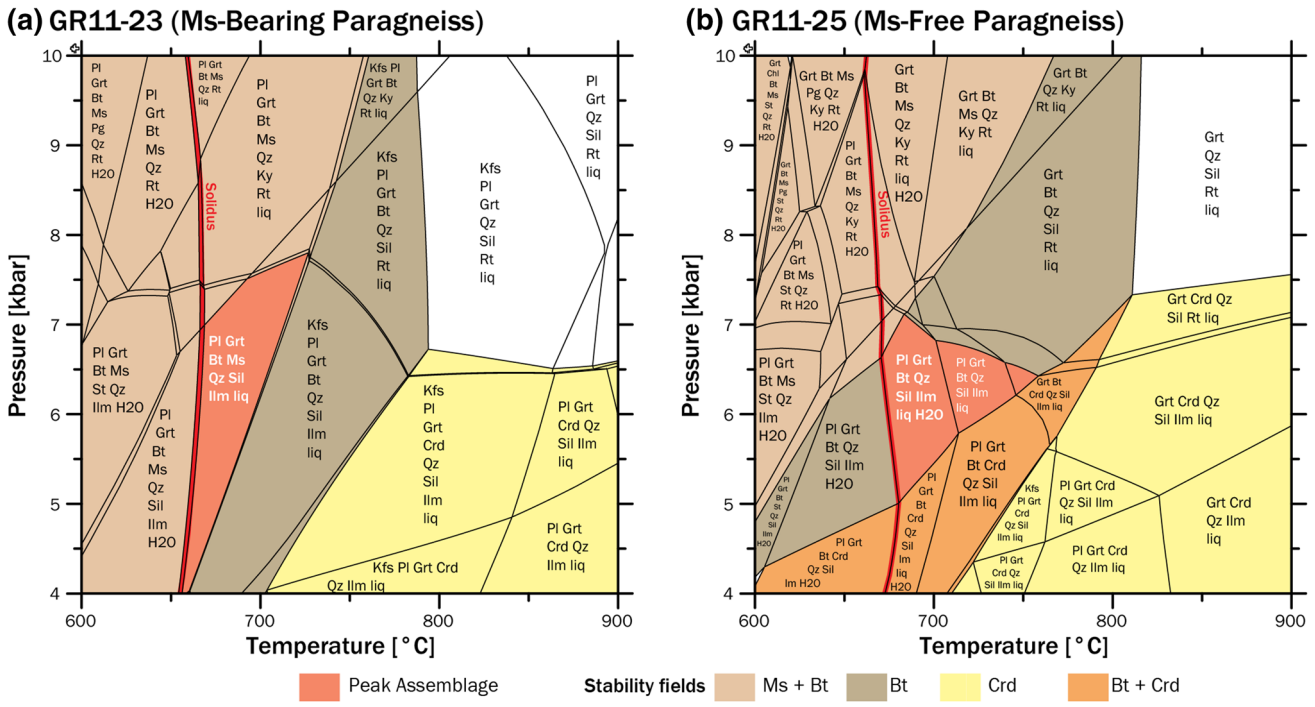

Fig. 9 Equilibrium phase diagrams calculated for migmatitic paragneiss samples: **a** Muscovite-bearing paragneiss sample GR11–23. **b** Muscovite-free paragneiss sample GR11–25

Discussion

Accuracy of P–T estimates

Determining the effective or equilibrium composition for a rock volume is probably the most challenging part of using quantitative petrology. This is especially true for rocks that have undergone partial melting, which can result in significant changes to the effective composition during prograde and retrograde metamorphism (e.g., Palin et al. 2016). However, we believe that our peak P–T estimates for the granulite samples are robust and accurate because there is considerable overlap in peak P–T estimates and derived P–T paths, whether we used whole rock compositions determined by XRF or compositions of microdomains determined by EPMA (Fig. 10). The starting point of the P–T paths shown in Fig. 8e–g is based on the composition of the garnet core in the microtexture from leucogranulite GR11–39. However, the effective bulk composition in which the garnet core formed may have been different from the measured composition. Therefore, the starting point of the P–T path may not be accurate, but we believe that it is a close approximation because textural evidence (i.e., sapphirine + orthopyroxene growth at the expense of garnet followed by formation of cordierite coronae) indicates that the residual granulite samples followed similar decompression-heating P- T paths (Fig. 8g, h) as the one derived from the garnet compositional isopleths for the leucogranulite shown in Fig. 8e.

For the migmatitic paragneiss samples, we used whole rock compositions to model peak P–T conditions, which have the risk of not representing the equilibrium composition. However, other studies (e.g., Hamilton and Pattison 2010; Koblinger and Pattison 2017) have shown that in rocks in which melt segregated from solids, using a non-equilibrium (whole rock) composition only affects the position of the melt-related quartz-, plagioclase-, and K-feldspar outlines and not the boundaries of the remnant solid phases. Therefore, we did not consider the stability of quartz or feldspars in estimating the peak P–T conditions and the presented peak P–T estimates should be accurate.

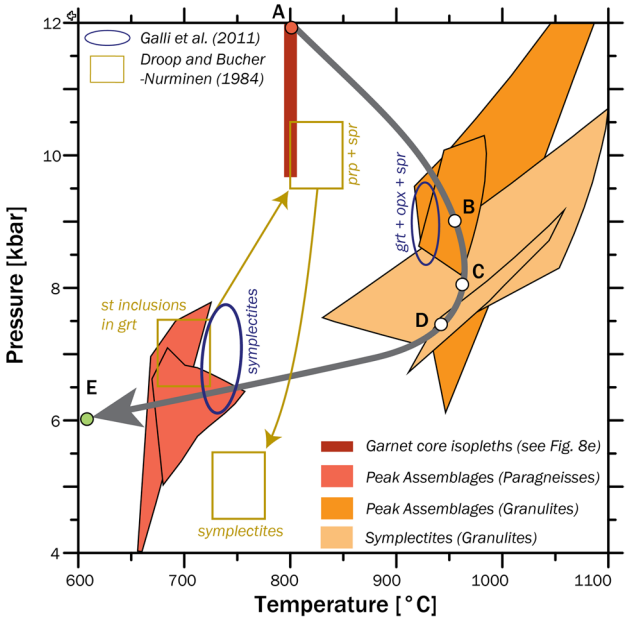

Fig. 10 P–T diagram showing estimates of peak metamorphic conditions for the granulites and paragneisses and a composite P–T path for the granulites. Points A, B, C, and D specify the P–T-path in Fig. 11

Protoliths of paragneisses and granulites

Based on the presence of Al-rich phases such as sillimanite and garnet (and muscovite in sample GR11-23), it is likely that the protoliths of the migmatitic paragneisses were pelitic rocks with various amounts of quartz. The protoliths of the granulites, however, are not as easily discerned. Based on the low abundances of quartz and feldspars and high Al and low Si concentrations (Online Resource Table S2), it is evident that the residual granulites lost melt at some point. All of the granulites contain Permian to Cretaceous, oscillatory-zoned zircon, which is interpreted to have crystallized from melt (Liati and Gebauer 2003; Nicollet et al. 2018), indicating that there was a higher proportion of melt in the residual granulites prior to Cenozoic time. Therefore, the residual granulites and melanosomes in the leucogranulites likely developed their restitic character, at least in part, prior to UHT metamorphism. The earlier melt-loss events preconditioned the granulites for the subsolidus reactions that took place at UHT conditions as described by Kelsey and Hand (2015). The presence of abundant high-Al phases (e.g., sillimanite, sapphirine, and garnet) and lack of high-Ca phases (e.g., orthopyroxene instead of clinopyroxene or amphibole) lead us to postulate the protoliths of the granulites and charnockites were also pelitic sedimentary rocks.

Composite pressure–temperature path

The conditions of a pre-peak high-pressure stage (ca. 800 °C and 9–12 kbar) are constrained by the garnet compositional isopleths from the leucogranulite sample GR11-39 (Fig. 8e). The garnet volume percent isopleths from the leucogranulite and residual granulite samples imply that the granulite/charnockite units were decompressed/exhumed to ca. 7 kbar while being heated to UHT conditions (Fig. 8f, g), resulting in sapphirine + orthopyroxene growth at the expense of garnet. The symplectite textures that replace garnet are also suggestive of a decompression P–T path. The rocks were

further decompressed into the stability field of cordierite + orthopyroxene for the residual granulites (less than ca. 8.5 kbar at 800–1000 °C) (Fig. 8g).

The granulite/charnockite units were then juxtaposed against the mid crustal migmatitic paragneisses, which were undergoing peak metamorphism at ca. 700–750 °C and 5–8 kbar. This implies a composite P–T path for the granulites and charnockites characterized by early decompression and heating, an intermediate, nearly isothermal decompression stage at UHT conditions, and finally cooling and decompression to the conditions recorded by the surrounding migmatites (Fig. 10).

Figure 11 shows the change in modal abundances of minerals in the granulites along the P–T path in Fig. 10 calculated with the P–T loop function of Theriak-Domino. For the garnet-breakdown texture from leucogranulite sample GR11-39, sapphirine was the first of the symplectite-forming minerals to grow at 950 °C and 9.2 kbar (Point B in Fig. 11a) as the modal abundance of garnet was slightly decreasing. This sluggish garnet-breakdown of the leucogranulite sample may explain why the metastable garnet core preserved the peak-pressure metamorphic-conditions in contrast to the garnets of the residual granulites. The garnet modal abundance of the residual granulites, which is obviously a function of the bulk rock composition, significantly decreased during heating (Point A–C in Fig. 11b, c). Up to 940 °C and 7.25 kbar (Point D in Fig. 11a), there was a sharp increase in the modes of orthopyroxene and spinel and decrease in sapphirine, indicating that sapphirine was partially consumed to form orthopyroxene + spinel. Residual granulite sample Gruf100 and Br03-56-2 behaved similarly with orthopyroxene and sapphirine modes increasing and garnet mode decreasing beginning at ca. 950 °C and 9.2 kbar (Point B in Fig. 11b, c). In addition, the modal abundance of sillimanite decreased as cordierite and sapphirine modes increased in the residual granulite sample. These patterns are consistent with the petrographic observations that orthopyroxene + sapphirine (+ cordierite in the residual granulites) grew at the expense of garnet at UHT conditions, indicating that the proposed P–T path is accurate.

Figure 10 shows no discrepancies between our UHT estimates and those of Galli et al. (2011), who also used the equilibrium phase diagram ("pseudosection") approach. The conditions of garnet breakdown and symplectite formation determined in this study contrast the estimates presented by Galli et al. (2011) of 700–750 °C and 6–8 kbar and by Droop and Bucher-Nurminen (1984) of 750 ± 100 °C and 5 ± 1 kbar, which were calculated by geothermobarometry for a fixed mineral assemblage. Based in part on these results, Galli et al. (2011) concluded that UHT metamorphism did not occur during Alpine orogenesis. Geothermobarometry could be useful when applied to low variance mineral assemblages. However, if one participating phase is

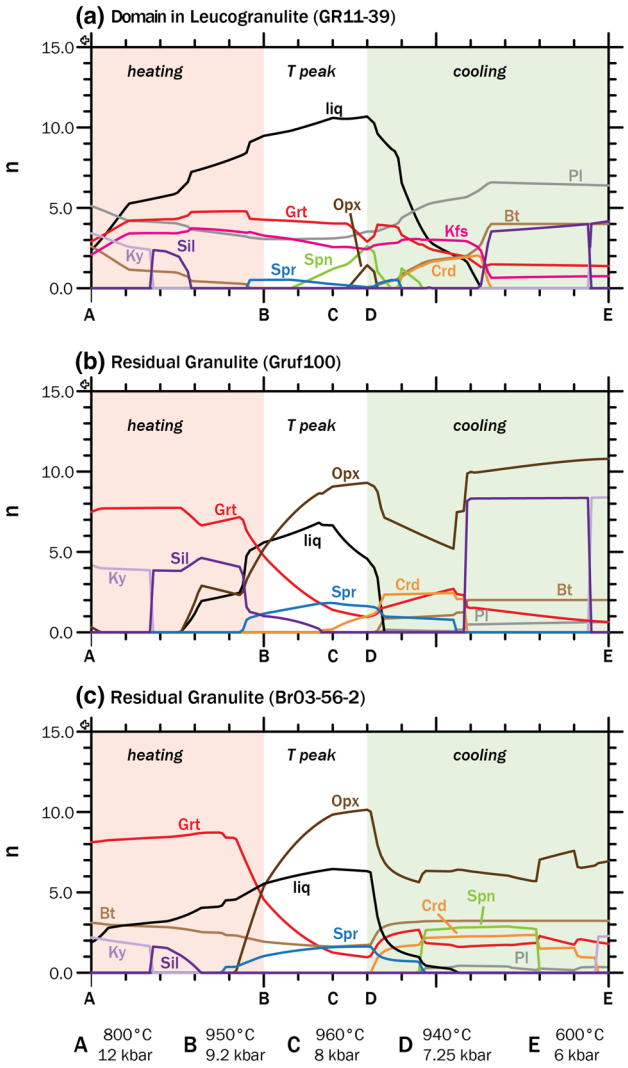

Fig. 11 Diagrams showing modal abundance changes of selected minerals along the P–T path shown in Fig. 10. **a** Leucogranulite GR11-39. **b** Residual granulite Gruf100. **c** Residual granulite Br03-56-2. Points A, B, C, and D correspond to the points on the P–T-path in Fig. 10

not taken into account, the results will be inaccurate. Thus, equilibrium phase diagrams and geothermobarometry can show different metamorphic conditions (stability field of equilibrium assemblage versus reactions between a set of equilibrated mineral phases; see also Lanari and Duesterhoeft 2019). The P–T conditions of the symplectite stage estimated by Galli et al. (2011) agree with our P–T estimates for the peak assemblage of the paragneiss samples, likely indicating that the compositions of garnet and other minerals were still open to modification by diffusion and reequilibration at post-UHT conditions. A possible interpretation is that our P–T estimates record the conditions at the onset of symplectite formation, whereas the estimates of Galli et al. (2011) for the symplectite stage record the P–T conditions of

the retrogressed matrix. We interpret our results to indicate that UHT conditions were reached during the latest metamorphic event, which occurred during Alpine orogenesis, at ca. 34 Ma (Liati and Gebauer 2003; Schmitz et al. 2009; Oalmann 2017; Nicollet et al. 2018). Furthermore, Galli et al. (2011, 2012) attributed UHT metamorphism to post-Variscan, Permian rifting of the European margin. However, isobaric cooling P–T paths are derived for UHT rocks from waning rift zones in most cases, whereas UHT decompression is more common in orogenic accretion and collision settings (Kelsey and Hand 2015). Therefore, we interpret the decompression-heating P–T path derived for the Gruf granulites in this study to indicate that UHT conditions were obtained in an orogenic setting (i.e., the Alpine orogeny).

Relating the P–T path to ages

Figure 12 shows a pressure–temperature–time path for the Gruf Complex based on the U-Pb ages of Oalmann (2017) and assuming that UHT metamorphism occurred during a single P–T event (Alpine) as discussed above. Rare earth element patterns of 34.8 ± 1.1 Ma zircon domains in the residual granulite indicate that this zircon grew in equilibrium with garnet and thus prior to garnet breakdown (Oalmann 2017). Therefore, we interpret this age to constrain

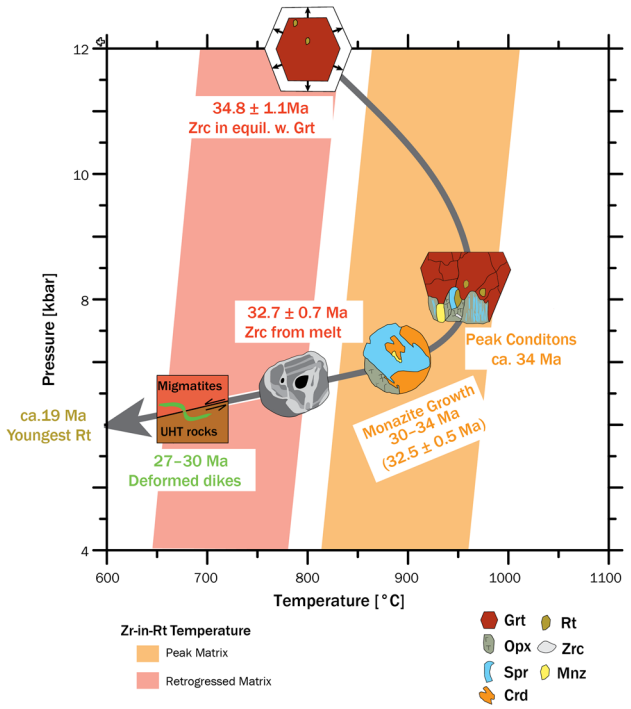

Fig. 12 Pressure–temperature diagram showing the pressure–temperature–time evolution of the Gruf granulites and migmatitic paragneisses with schematic mineral reactions and structural events. Zr-in-rutile temperatures and U-Pb rutile age; monazite and zircon ages are from Oalmann (2017)

the timing of the pre-peak, high-pressure stage (Fig. 12). The next younger zircon population crystallized from post-UHT melts in the leucogranulite at 32.7 ± 0.7 Ma (Liati and Gebauer 2003; Oalmann 2017), after garnet breakdown as indicated by steep REE-patterns with high HREE concentrations (Oalmann 2017). This leads to the interpretation that UHT metamorphism likely occurred between 34.8 ± 1.1 Ma and 32.7 ± 0.7 Ma (Fig. 12). A ca. 34 Ma age for UHT metamorphism is also consistent with monazite ages of 33.0 ± 4.4 Ma (Schmitz et al. 2009) and 31.8 ± 0.3 Ma (Nicollet et al. 2018). A monazite inclusion in a slightly post-peak sapphirine + cordierite-bearing domain (= sample GRM-37), which equilibrated at > 850 °C and > 7 kbar (Fig. 8d), yielded an age of 32.5 ± 0.5 Ma (Oalmann 2017). Because the migmatites were undergoing ductile deformation when the lower crustal charnockites and granulites were exhumed into the middle crust between 30 and 27 Ma, we interpret that the P–T conditions estimated for the paragneiss samples (675–750 °C and 5–7 kbar) (Fig. 9) represent the conditions of the middle crust into which the lower crustal rocks were exhumed. The ages of undeformed, muscovite-rich dikes and plutons indicate that contractional deformation ended and the amalgamated Gruf Complex was being exhumed between 26 and 24 Ma (Oalmann 2017). U-Pb rutile ages indicate that the Gruf granulites and charnockites underwent cooling from 700 to 420 °C between 30 and 19 Ma (Oalmann 2017).

High-temperature metamorphism in other parts of the Central Alps

The 32–22 Ma (Rubatto et al. 2009; Berger et al. 2011) Barrovian metamorphism of the Lepontine Dome ranged from greenschist-facies metamorphism to sillimanite-zone migmatization (Todd and Engi 1997; Frey and Ferreiro Mählmann 1999; Burri et al. 2005). The P–T conditions that we estimate for the migmatitic paragneisses (650–750 °C and 5–7 kbar) are consistent with the P–T conditions of muscovite dehydration melting in the Southern Steep Belt of 650–750 °C and 6–8 kbar (Burri et al. 2005). This indicates that the middle crust of a large part of the southern Central Alps experienced high-temperature metamorphism coeval with and subsequent to UHT metamorphism of the lower crust.

In a recent study, Tumiati et al. (2018) reported the presence of sapphirine-bearing symplectites in eclogites and peridotites from the Monte Duria area of the Adula nappe that formed at 810–850 °C and 8–10 kbar. Although these authors did not assign an age to the symplectite formation, textural evidence indicates that these textures formed after eclogite facies metamorphism. This is the first mention of sapphirine in the Central Alps outside of the Gruf Complex and, thus, it is possible that the Adula nappe also underwent

near-UHT metamorphism following Alpine high-pressure metamorphism. However, Tumiati et al. (2018) do not rule out that both the high-pressure and high-temperature events occurred prior to Alpine orogenesis.

Geodynamic model for the Central Alps

Any valid tectonometamorphic model for the Gruf Complex must consider the P–T–t path shown in Fig. 12. One such scenario is that the lower crustal granulites and charnockites were subducted or buried to depths equivalent to 9–12 kbar (ca. 32–42 km) and subsequently exhumed to 7.5–9.5 kbar (ca. 25–33 km depth) while being heated by advected mantle. The switch from the short-termed, nearly isothermal decompression at ca. 34 Ma to decompression + cooling (Figs. 8, 10, 12) may have been the result of the granulites and charnockites retaining heat while being exhumed to depths equivalent to less than 7 kbar within the crust.

The tectonometamorphic evolution of the Gruf Complex discussed above must be represented in viable geodynamic models for the Central Alps. Accordingly, a valid model must account for (1) (U)HP metamorphism at 40–35 Ma (Gebauer 1996; Brouwer et al. 2005; Hermann et al. 2006; Sandmann et al. 2014) followed by (2) Barrovian metamorphism (beginning at ca. 32 Ma; Rubatto et al. 2009) of the Adula nappe and other units of the Lepontine Dome, and (3) petrogenesis of the magmas that formed the Periadriatic intrusions (e.g., the Biella, Bergell, Adamello, and Riesenferner intrusions), which intruded the Western, Central and Eastern Alps between 34 and 28 Ma (e.g., von Blanckenburg and Davies 1995; Rosenberg 2004; Samperton et al. 2015). Based on U-Pb geochronological constraints, a valid model must also account for partial exhumation of the (U)HP units prior to ca. 34 Ma (Gebauer 1996; Hermann et al. 2006). Two previously published geodynamic models could possibly produce the observations noted here: (1) Slab breakoff (e.g., von Blanckenburg and Davies 1995; Handy et al. 2010) leads to buoyant exhumation of the (U)HP units (subducted Penninic units and European margin, i.e., the Adula Nappe) followed by infiltration of asthenospheric mantle into the gap, UHT metamorphism in the Gruf-complex, exhumation of the Gruf-complex and the Chiavenna oceanic unit (Schmutz 1976), and emplacement of the Bergell magmas. (2) Slab rollback of the Valaisan slabs leads to lithospheric thinning (Beltrando et al. 2010), resulting in exhumation of the (U)HP units along lithospheric-scale faults followed by upwelling of the asthenosphere, which leads to adiabatic melting in the lithospheric mantle and UHT metamorphism in the lower crust, and finally a switch back to contractional deformation. However, we prefer the slab breakoff model because the lithospheric thinning model of Beltrando et al. (2010) does not accurately portray the timing of the Bergell intrusion and there is no evidence for large-scale north–south extension (i.e., no trench-directed extension exists that would point to slab rollback) within the Central Alps. However, two east–west extensional shear zones exist that terminate close to the Gruf: the Turba Mylonite Zone of Nievergelt et al. (1996) and the Martegnas Shear Zone of Weh and Froitzheim (2001). The timing of both shear zones is close to 34 Ma.

Figure 13 schematically shows our proposed model for the geodynamic evolution of the Central Alps based on the results of this study and models presented by Schmid et al. (1996), Bousquet et al. (2002), Goffé et al. (2003), Handy et al. (2010), and Pfiffner (2016). Figure 13 shows the situation after the subduction stage of the Alpine orogeny that resulted in (U)HP metamorphism of the Adula and Penninic nappes between 45 and 35 Ma (e.g., Becker 1993; Gebauer 1996; Bousquet et al. 2002; Hermann et al. 2006). During this time period, the Gruf Complex, interpreted to be of European margin affinity (Bousquet et al. 2012b; Galli et al. 2012), was likely being thrust beneath the Austroalpine nappe stack and amalgamated with the Penninic nappes.

At ca. 34 Ma, the Gruf Complex was undergoing UHT metamorphism at 900–1000 °C and 7.5–9.5 kbar (25–33 km depth) following decompression from 800 °C and 10–13 kbar (35–45 km depth) at ca. 35 Ma (Figs. 12, 13a). The lack of a UHT overprint on the Adula and Penninic units implies that these units had been exhumed above the European margin prior to slab breakoff at 34 Ma (Fig. 13a).

Between 30 and 27 Ma, the Gruf granulites and charnockites were exhumed into the middle crust (Oalmann 2017) (Fig. 13b). Amalgamation of the Gruf Complex was coeval with the last stages of crystallization of the Bergell intrusion (black-white cross pattern in Fig. 13), indicating that exhumation of the granulites may have been assisted by the buoyantly intruding Bergell massif.

Between 26 and 24 Ma, the crustally derived Novate leucogranite and associated muscovite-rich dikes intruded the Gruf Complex (Liati et al. 2000; Oalmann 2017). We interpret this to indicate that exhumation of the amalgamated Gruf Complex along the Insubric line occurred then and was likely a result of wedging of Apulian lower crust (Fig. 13c) during the continent–continent collision, which also cut the supply of mantle-derived magmas to the Gruf Complex. Slip along the normal sense Forcola Fault occurred coevally with intrusion of the Novate leucogranite at ca. 24 Ma, exhuming the Adula nappe relative to the Gruf Complex (Ciancaleoni and Marquer 2006).

Comparison of the Central Alps with cenozoic convergent settings

Ultra-high temperature rocks have been discovered in other Cenozoic convergent tectonic settings. For example, UHT xenoliths were entrained in lavas that erupted on the Pamir

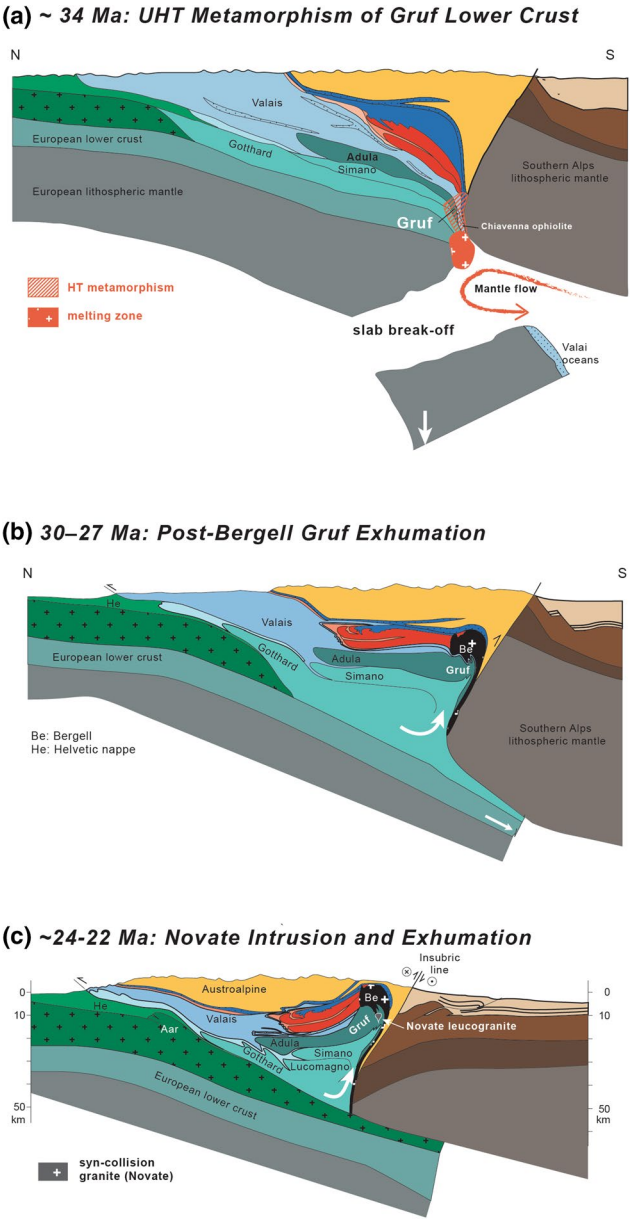

Fig. 13 Schematic model for the geodynamic evolution of the Central Alps (after Schmid et al. 1996; Goffé et al. 2003). **a** ca. 34 Ma: UHT metamorphism of the Gruf crustal rocks following slab breakoff at the ***O****cean*(Valais)-***C****ontinent*(Europa) ***T****ransition* and partial melting of the *OCT* (future Bergell). **b** 30–27 Ma: exhumation of the Gruf Complex closely following intrusion of the Bergell tonalite and granodiorite. **c** ca. 24 Ma: further exhumation of the amalgamated Gruf Complex and the Bergell intrusion along the Insubric line, intrusion of the Novate leucogranite, and onset of continent–continent collision. The legend is the same as in Fig. 1

(Gordon et al. 2012) and Tibetan (Hacker et al. 2000) Plateaus, and UHT granulites crop out on Seram Island within the Banda Arc in Indonesia (Pownall et al. 2014). The Pamir xenoliths were subjected to higher pressures (≥ 15 to 20 kbar) (Gordon et al. 2012) than the Gruf granulites, whereas the Tibetan xenoliths underwent UHT metamorphism at 8–12 kbar (Hacker et al. 2000). Proposed geodynamic models for UHT metamorphism of the Tibetan lower crust include lithospheric thinning, slab breakoff, and continental subduction. Pownall et al. (2014) concluded that UHT metamorphism in eastern Indonesia resulted from exhumation of lithospheric mantle into the lower crust during a period of extreme extension driven by slab rollback in the Banda Arc. The Alpine orogeny is different from the Pamir-Tibet and Indonesian examples in that the oceanic subduction stage was not long lived in the Alps.

All these models invoke advection of hot mantle material into the crust resulting in UHT metamorphism. Therefore, UHT metamorphism can occur in convergence settings if there are slab breakoff, mantle upwelling or episodes of lithospheric-scale extension. This may imply that UHT metamorphism is more common in Phanerozoic collisional orogens than previously thought. The products of these extreme thermal processes may not be exposed or not recognized as UHT rocks due to retrograde overprinting or bulk compositions that do not produce obvious UHT assemblages (e.g., sapphirine + quartz).

Conclusions

Thermodynamic modeling of whole-rock and microdomain (reaction texture) compositions from leucocratic as well as restitic granulites yields petrologically reasonable results if the effective reaction composition is determined. The modeled P–T path indicates that the granulite/charnockite units of the Gruf Complex reached UHT conditions (ca. 900–1000 °C and 7.0–9.5 kbar) during decompression from 9 to 12 kbar and ca. 800 °C at ca. 34 Ma, leading to sapphirine + orthopyroxene growth at the expense of garnet in all granulite types. The lower crustal UHT rocks were further decompressed to < 7 kbar at (near) UHT temperatures and subsequently juxtaposed against midcrustal migmatitic gneisses, which underwent peak metamorphism at 700–750 °C and 5–8 kbar, by between 30 and 27 Ma.

The decompression-heating P–T path experienced by the granulites and charnockites of the Gruf Complex likely was the result of the slab breakoff that is coeval with the switch from subduction to collision at ca. 34 Ma within the Central Alps. The Gruf UHT rocks are most likely somewhat analogous to UHT rocks from other Cenozoic convergent settings including the Tibetan plateau and the Banda Arc in Indonesia.

Acknowledgements This research is supported by the American National Science Foundation under Grant no. EAR 0911633 to A. Möller. We would like to thank (A) Galli for guiding us in the field area, the Biavaschi family at Rifugio Brasca for their hospitality and logistical help, P.G. Lippert for field assistance, and C. Fischer

(University of Potsdam) and W.C. Dickerson (University of Kansas) for preparing thin sections. P. Appel and (B) Mader (University of Kiel) and (C) Gunther and M. Konrad-Schmolke (University of Potsdam) assisted with the EPMA work. We are also grateful to A. Galli, V. Guevara, M. Caddick, and several others for fruitful discussions about the Gruf Complex. Sebastian Weber, Niko Froitzheim, and an anonymous colleague are thanked for their thoughtful and critical reviews.

References

Armstrong JT (1995) CITZAF-a package of correction programs for the quantitative electron microbeam X-ray-analysis of thick polished materials, thin-films, and particles. Microbeam Anal 4(3):177–200

Becker H (1993) Garnet peridotite and eclogite Sm-Nd mineral ages from the Lepontine dome (Swiss Alps): new evidence for Eocene high-pressure metamorphism in the central Alps. Geology 21(7):599–602

Beltrando M, Lister GS, Rosenbaum G, Richards S, Forster MA (2010) Recognizing episodic lithospheric thinning along a convergent plate margin: the example of the Early Oligocene Alps. Earth Sci Rev 103(3):81–98

Berger A, Bousquet R (2008) Subduction-related metamorphism in the Alps: review of isotopic ages based on petrology and their geodynamic consequences. Geol Soc Lond Spec Publ 298(1):117–144

Berger A, Rosenberg C, Schmid S (1996) Ascent, emplacement and exhumation of the Bergell pluton within the Southern Steep Belt of the Central Alps. Schweiz Mineral Petrogr Mitt 76(3):357–382

Berger A, Schmid SM, Engi M, Bousquet R, Wiederkehr M (2011) Mechanisms of mass and heat transport during Barrovian metamorphism: a discussion based on field evidence from the Central Alps (Switzerland/northern Italy). Tectonics 30:TC1007

Blackburn T, Shimizu N, Bowring SA, Schoene B, Mahan KH (2012) Zirconium in rutile speedometry: new constraints on lower crustal cooling rates and residence temperatures. Earth Planet Sci Lett 317:231–240

Bousquet R, Goffé B, Vidal O, Oberhänsli R, Patriat M (2002) The tectono-metamorphic history of the Valaisan domain from the Western to the Central Alps: new constraints on the evolution of the Alps. Geol Soc Am Bull 114(2):207–225

Bousquet R, Oberhänsli R, Schmid SM et al (2012a) Metamorphic framework of the Alps, Commission for the Geological Map of the World, CCGM/CGMW

Bousquet R, Schmid SM, Zeilinger G et al (2012b) Tectonic framework of the Alps, Commission for the Geological Map of the World, CCGM/CGMW

Brouwer F, Burri T, Engi M, Berger A (2005) Eclogite relics in the Central Alps: PT- evolution, Lu-Hf ages, and implications for formation of tectonic mélange zones. Schweiz Mineral Petrogr Mitt 85:147–174

Brown M (2006) Duality of thermal regimes is the distinctive characteristic of plate tectonics since the Neoarchean. Geology 34(11):961–964

Brown M (2007) Metamorphic conditions in orogenic belts: a record of secular change. Int Geol Rev 49(3):193–234

Bucher-Nurminen K, Droop G (1983) The metamorphic evolution of garnet-cordierite-sillimanite-gneisses of the Gruf-Complex, Eastern Pennine Alps. Contrib Mineral Petrol 84:215–227

Burri T, Berger A, Engi M (2005) Tertiary migmatites in the Central Alps: regional distribution, field relations, conditions of formation, and tectonic implications. Schweiz Mineral Petrogr Mitt 85(2–3):215–232

Carswell D, O'Brien P (1993) Thermobarometry and geotectonic significance of high-pressure granulites: examples from the Moldanubian Zone of the Bohemian Massif in Lower Austria. J Petrol 34(3):427–459

Ciancaleoni L, Marquer D (2006) Syn-extension leucogranite deformation during convergence in the Eastern Central Alps: example of the Novate intrusion. Terra Nova 18(3):170–180

Clark C, Fitzsimons IC, Healy D, Harley SL (2011) How does the continental crust get really hot? Elements 7(4):235–240

Coggon R, Holland T (2002) Mixing properties of phengitic micas and revised garnet-phengite thermobarometers. J Metamorph Geol 20(7):683–696

Collins W (2002) Hot orogens, tectonic switching, and creation of continental crust. Geology 30(6):535–538

Davidson C, Rosenberg C, Schmid S (1996) Symmagmatic folding of the base of the Bergell pluton, Central Alps. Tectonophysics 265(3):213–238

De Capitani C (1994) Gleichgewichts-phasendiagramme: theorie und software. Beiheft zur Deutschen Mineralogischen Gesellschaft 6:1–48

De Capitani C, Petrakakis K (2010) The computation of equilibrium assemblage diagrams with Theriak/Domino software. Am Mineral 95(7):1006–1016

Diener J, Powell R (2012) Revised activity—composition models for clinopyroxene and amphibole. J Metamorph Geol 30(2):131–142

Dobrzhinetskaya L, Schweinehage R, Massonne HJ, Green H (2002) Silica precipitates in omphacite from eclogite at Alpe Arami, Switzerland: evidence of deep subduction. J Metamorph Geol 20(5):481–492

Droop GTR, Bucher-Nurminen K (1984) Reaction textures and metamorphic evolution of sapphirine-bearing granulites from the Gruf Complex, Italian Central Alps. J Petrol 25(3):766–803

Engi M, Berger A, Roselle GT (2001) Role of the tectonic accretion channel in collisional orogeny. Geology 29(12):1143–1146

Fitzsimons ICW, Harley SL (1994) The influence of retrograde cation exchange on granulite PT estimates and a convergence technique for the recovery of peak metamorphic conditions. J Petrol 35(2):543–576

Frey M, Ferreiro Mählmann R (1999) Alpine metamorphism of the Central Alps. Schweiz Mineral Petrogr Mitt 79(1):135–154

Galli A (2010) Tectonometamorphic evolution of the Gruf Complex (Swiss and Italian Central Alps). Dissertation, ETH Zürich

Galli A, Le Bayon B, Schmidt MW et al (2011) Granulites and charnockites of the Gruf Complex: evidence for Permian ultrahigh temperature metamorphism in the Central Alps. Lithos 124(1–2):17–45

Galli A, Le Bayon B, Schmidt MW et al (2012) U–Pb zircon dating of the Gruf Complex: disclosing the late Variscan granulitic lower crust of Europe stranded in the Central Alps. Contrib Mineral Petrol 163:353–378

Galli A, Le Bayon B, Schmidt MW, Burg J-P, Reusser E (2013) Tectonometamorphic history of the Gruf complex (Central Alps): exhumation of a granulite–migmatite complex with the Bergell pluton. Swiss J Geosci 106(1):33–62

Gebauer D (1996) A P–T–t path for an (Ultra?-) high-pressure ultramafic/mafic rock-association and its felsic country-rocks based on SHRIMP-dating of magmatic and metamorphic zircon domains. In: Example: Alpe Arami (Central Swiss Alps), earth processes: reading the isotopic code. Geophys Monogr Ser AGU, Washington, DC, pp 307–329

Goffé B, Bousquet R, Henry, Le Pichon X (2003) Effect of the chemical composition of the crust on the metamorphic evolution of orogenic wedges. J Metamorph Geol 21:123–141

Gordon S et al (2012) The thermal structure of continental crust in active orogens: insight from Miocene eclogite and granulite xenoliths of the Pamir Mountains. J Metamorph Geol 30(4):413–434

Guevara V, Caddick M (2016) Shooting at a moving target: phase equilibria modelling of high-temperature metamorphism. J Metamorph Geol 34:209–235

Guillong M, Hametner K, Reusser E, Wilson SA, Günther D (2005) Preliminary characterisation of new glass reference materials (GSA-1G, GSC-1G, GSD-1G and GSE-1G) by laser ablation-inductively coupled plasma-mass spectrometry using 193 nm, 213 nm and 266 nm wavelengths. Geostand Geoanalyt Res 29(3):315–331

Hacker BR, Gnos E, Ratschbacher L et al (2000) Hot and dry deep crustal xenoliths from Tibet. Science 287(5462):2463–2466

Hamilton BM, Pattison DR (2010) Thermodynamic modelling of open-system behaviour for anatectic metapelites. In: GeoCanada 2010—working with the earth

Handy MR, Schmid SM, Bousquet R, Kissling E, Bernoulli D (2010) Reconciling plate-tectonic reconstructions of Alpine Tethys with the geological–geophysical record of spreading and subduction in the Alps. Earth Sci Rev 102(3):121–158

Harley SL (1998) On the occurrence and characterization of ultrahigh-temperature crustal metamorphism. Geol Soc Lond Spec Publ 138(1):81–107

Harley SL (2008) Refining the P–T records of UHT crustal metamorphism. J Metamorph Geol 26(2):125–154

Heinrich CA (1986) Eclogite facies regional metamorphism of hydrous mafic rocks in the Central Alpine Adula Nappe. J Petrol 27(1):123–154

Hermann J, Rubatto D, Trommsdorff V (2006) Sub-solidus Oligocene zircon formation in garnet peridotite during fast decompression and fluid infiltration (Duria, Central Alps). Mineral Petrol 88(1):181–206

Herwartz D, Münker C, Scherer EE, Nagel TJ, Pleuger J, Froitzheim N (2008) Lu-Hf garnet geochronology of eclogites from the Balma Unit (Pennine Alps): implications for Alpine paleotectonic reconstructions. In: Froitzheim N, Schmid SM (eds) Orogenic processes in the Alpine collision zone, Swiss journal of geosciences supplement, vol 3. Birkhäuser, Basel, pp S173–S189

Holland TJB, Powell R (1998) An internally consistent thermodynamic data set for phases of petrological interest. J Metamorph Geol 16(3):309–343

Holland TJB, Powell R (2003) Activity–composition relations for phases in petrological calculations: an asymmetric multicomponent formulation. Contrib Mineral Petrol 145(4):492–501

Jochum KP, Willbold M, Raczek I, Stoll B, Herwig K (2005) Chemical characterisation of the USGS reference glasses GSA-1G, GSC-1G, GSD-1G, GSE-1G, BCR-2G, BHVO-2G and BIR-1G Using EPMA, ID-TIMS, ID-ICP-MS and LA-ICP-MS. Geostand Geoanalyt Res 29(3):285–302

Johnson D, Hooper P, Conrey R (1999) XRF analysis of rocks and minerals for major and trace elements on a single low dilution Li-tetraborate fused bead. In: Le Bas M (ed) Advances in X-ray analysis, pp 843–867

Kelsey DE (2008) On ultrahigh-temperature crustal metamorphism. Gondwana Res 13(1):1–29

Kelsey DE, Hand M (2015) On ultrahigh temperature crustal metamorphism: phase equilibria, trace element thermometry, bulk composition, heat sources, timescales and tectonic settings. Geosci Front 6(3):311–356

Kelsey DE, White RW, Holland TJB, Powell R (2004) Calculated phase equilibria in K_2O-FeO-MgO-Al_2O_3-SiO_2-H_2O for sapphirine-quartz-bearing mineral assemblages. J Metamorph Geol 22(6):559–578

Koblinger BM, Pattison DRM (2017) Crystallization of heterogeneous pelitic migmatites: insights from thermodynamic modelling. J Petrol 58:297–326

Kooijman E, Smit M, Mezger K, Berndt J (2012) Trace element systematics in granulite facies rutile: implications for Zr geothermometry and provenance studies. J Metamorph Geol 30(4):397–412

Krogh Ravna E, Terry MP (2004) Geothermobarometry of UHP and HP eclogites and schists—an evaluation of equilibria among garnet–clinopyroxene–kyanite–phengite–coesite/quartz. J Metamorph Geol 22(6):579–592

Lanari P, Duesterhoeft E (2019) Modeling metamorphic rocks using equilibrium thermodynamics and internally consistent databases: past achievements, problems and perspectives. J Petrol 60(1):19–56

Liati A, Gebauer D (2003) Geochronological constraints for the time of metamorphism in the Gruf Complex (Central Alps) and implications for the Adula-Cima Lunga nappe system. Schweiz Mineral Petrogr Mitt 83:159–172

Liati A, Gebauer D, Fanning M (2000) U-Pb SHRIMP dating of zircon from the Novate granite (Bergell, Central Alps): evidence for Oligocene-Miocene magmatism, Jurassic/Cretaceous continental rifting and opening of the Valais trough. Schweiz Mineral Petrogr Mitt 80(3):305–316

Luvizotto G, Zack T, Meyer HP et al (2009) Rutile crystals as potential trace element and isotope mineral standards for microanalysis. Chem Geol 261(3):346–369

Nicollet C, Bosse V, Spalla MI, Schiavi F (2018) Eocene ultra high temperature (UHT) metamorphism in the Gruf complex (Central Alps): constraints by LA-ICPMS zircon and monazite dating in petrographic context. J Geol Soc Lond 175(5):774–787

Nievergelt P, Liniger M, Froitzheim N, Mählmann RF (1996) Early to mid Tertiary crustal extension in the Central Alps: the Turba Mylonite Zone (Eastern Switzerland). Tectonics 15(2):329–340

O'Brien PJ (2008) Challenges in high-pressure granulite metamorphism in the era of pseudosections: reaction textures, compositional zoning and tectonic interpretation with examples from the Bohemian Massif. J Metamorph Geol 26(2):235–251

Oalmann J (2017) Integrating in situ geochronology and metamorphic petrology: an example from the Gruf Complex, European Central Alps. Dissertation, The University of Kansas. https://kuscholarworks.ku.edu/handle/1808/26345

Palin RM, Weller OM, Waters DJ, Dyck B (2016) Quantifying geological uncertainty in metamorphic phase equilibria modelling; a Monte Carlo assessment and implications for tectonic interpretations. Geosci Front 7(4):591–607. https://doi.org/10.1016/j.gsf.2015.08.005

Paton C, Hellstrom J, Paul B, Woodhead J, Hergt J (2011) Iolite: freeware for the visualisation and processing of mass spectrometric data. J Anal At Spectrom 26(12):2508–2518

Pattison DRM, Chacko T, Farquhar J, McFarlane CR (2003) Temperatures of granulite-facies metamorphism: constraints from experimental phase equilibria and thermobarometry corrected for retrograde exchange. J Petrol 44(5):867–900

Pfiffner OA (2016) Basement-involved thin-skinned and thick-skinned tectonics in the Alps. Geol Mag 153(5/6):1085–1109

Pownall JM, Hall R, Armstrong RA, Forster MA (2014) Earth's youngest known ultrahigh-temperature granulites discovered on Seram, eastern Indonesia. Geology 42(4):279–282

Rosenberg C (2004) Shear zones and magma ascent: a model based on a review of the Tertiary magmatism in the Alps. Tectonics 23(TC3002):1–21

Rubatto D, Hermann J, Berger A, Engi M (2009) Protracted fluid-induced melting during Barrovian metamorphism in the Central Alps. Contrib Mineral Petrol 158(6):703–722

Samperton KM, Schoene B, Cottle JM et al (2015) Magma emplacement, differentiation and cooling in the middle crust: integrated zircon geochronological–geochemical constraints from the Bergell Intrusion, Central Alps. Chem Geol 417:322–340

Sandmann S, Nagel TJ, Herwartz D, Fonseca ROC, Kurzawski RM, Münker C, Froitzheim N (2014) Lu-Hf garnet systematics of a polymetamorphic basement unit: new evidence for coherent exhumation of the Adula Nappe (Central Alps) from eclogite-facies conditions. Contrib Mineral Petrol 168:1075

Schefer S (2005) Metamorphose und Deformation im Gruf-Komplex, Val Codera, Italien. Diploma Thesis, University of Basel

Schmid SM, Pfiffner O-A, Froitzheim N, Schönborn G, Kissling E (1996) Geophysical-geological transect and tectonic evolution of the Swiss–Italian Alps. Tectonics 15(5):1036–1064

Schmitz S, Möller A, Wilke M, Malzer W, Kanngiesser B, Bousquet R, Berger A, Schefer S (2009) Chemical U-Th-Pb dating of monazite by 3D-Micro X-ray fluorescence analysis with synchrotron radiation. Eur J Mineral 21(5):927–945. https://doi.org/10.1127/0935-1221/2009/0021-1964

Schmutz H-U (1976) Der Mafitit-Ultramafitit-Komplex zwischen Chiavenna und Val Bondasca. Beiträge zur Geologischen Karte der Schweiz 149:73

Sizova E, Gerya T, Brown M, Perchuk L (2010) Subduction styles in the Precambrian: insight from numerical experiments. Lithos 116(3):209–229

Stampfli GM, Mosar J, Marquer D et al (1998) Subduction and obduction processes in the Swiss Alps. Tectonophysics 296(1):159–204

Todd CS, Engi M (1997) Metamorphic field gradients in the Central Alps. J Metamorph Geol 15(4):513–530

Trommsdorff V (1990) Metamorphism and tectonics in the Central Alps: the Alpine lithospheric mélange of Cima Lunga and Adula. Memorie della Società Geologica Italiana 45:39–49

Tumiati S, Zanchetta S, Pellegrino L, Ferrario C, Casartelli S, Malaspina N (2018) Granulite-facies overprint in garnet peridotites and kyanite eclogites of Monte Duria (Central Alps, Italy): clues from srilankite- and sapphirine-bearing symplectites. J Petrol 59(1):115–152

Von Blanckenburg F (1992) Combined high-precision chronometry and geochemical tracing using accessory minerals: applied to the Central-Alpine Bergell intrusion (central Europe). Chem Geol 100(1–2):19–40

Von Blanckenburg F, Davies JH (1995) Slab breakoff: a model for syncollisional magmatism and tectonics in the Alps. Tectonics 14(1):120–131

Watson E, Wark D, Thomas J (2006) Crystallization thermometers for zircon and rutile. Contrib Mineral Petrol 151(4):413–433

Weh M, Froitzheim N (2001) Penninic cover nappes in the Prättigau half-window (Eastern Switzerland): structure and tectonic evolution. Eclogae Geol Helv 94:237–252

White RW, Powell R, Clarke G (2002) The interpretation of reaction textures in Fe-rich metapelitic granulites of the Musgrave Block, central Australia: constraints from mineral equilibria calculations in the system K_2O–FeO–MgO–Al_2O_3–SiO_2–H_2O–TiO_2–Fe_2O_3. J Metamorph Geol 20(1):41–55

White RW, Pomroy NE, Powell R (2005) An in situ metatexite–diatexite transition in upper amphibolite facies rocks from Broken Hill, Australia. J Metamorph Geol 23(7):579–602

White RW, Powell R, Holland TJB (2007) Progress relating to calculation of partial melting equilibria for metapelites. J Metamorph Geol 25(5):511–527